ARTICLE

doi:10.1038/nature16071

Brain tumour cells interconnect to a functional and resistant network

Matthias Osswald[1,2], Erik Jung[1,2]*, Felix Sahm[3,4]*, Gergely Solecki[1,2]*, Varun Venkataramani[5], Jonas Blaes[1,2], Sophie Weil[1,2], Heinz Horstmann[5], Benedikt Wiestler[1,2,6], Mustafa Syed[1,2], Lulu Huang[1,2], Miriam Ratliff[2,7], Kianush Karimian Jazi[1,2], Felix T. Kurz[8], Torsten Schmenger[1,2], Dieter Lemke[1,2], Miriam Gömmel[1,2], Martin Pauli[9], Yunxiang Liao[1,2], Peter Häring[10], Stefan Pusch[3,4], Verena Herl[11], Christian Steinhäuser[11], Damir Krunic[12], Mostafa Jarahian[13], Hrvoje Miletic[14], Anna S. Berghoff[15], Oliver Griesbeck[16], Georgios Kalamakis[17], Olga Garaschuk[17], Matthias Preusser[18], Samuel Weiss[19,20,21], Haikun Liu[22], Sabine Heiland[8], Michael Platten[1,23], Peter E. Huber[24,25], Thomas Kuner[5], Andreas von Deimling[3,4], Wolfgang Wick[1,2] & Frank Winkler[1,2]

Astrocytic brain tumours, including glioblastomas, are incurable neoplasms characterized by diffusely infiltrative growth. Here we show that many tumour cells in astrocytomas extend ultra-long membrane protrusions, and use these distinct tumour microtubes as routes for brain invasion, proliferation, and to interconnect over long distances. The resulting network allows multicellular communication through microtube-associated gap junctions. When damage to the network occurred, tumour microtubes were used for repair. Moreover, the microtube-connected astrocytoma cells, but not those remaining unconnected throughout tumour progression, were protected from cell death inflicted by radiotherapy. The neuronal growth-associated protein 43 was important for microtube formation and function, and drove microtube-dependent tumour cell invasion, proliferation, interconnection, and radioresistance. Oligodendroglial brain tumours were deficient in this mechanism. In summary, astrocytomas can develop functional multicellular network structures. Disconnection of astrocytoma cells by targeting their tumour microtubes emerges as a new principle to reduce the treatment resistance of this disease.

Astrocytomas (World Health Organisation grades II, III and IV; grade IV are called glioblastomas) are prototypical examples for highly invasive tumours that diffusely colonize their host organ[1], which ultimately leads to neurological dysfunction and death despite intensive radio- and chemotherapy. Oligodendroglioma is another glioma type that shares many molecular features like frequent isocitrate dehydrogenase (*IDH1* and *IDH2*) mutations[2,3], but is less invasive and far more vulnerable to therapeutic intervention than astrocytomas. A codeletion of the chromosomal parts 1p and 19q is characteristic for oligodendrogliomas, but absent in astrocytomas[2–4]. This codeletion allows for molecular subgrouping[2–4], and is associated with a high responsiveness of oligodendrogliomas to radiochemotherapy, leading to marked long-term survival benefits[5,6]. The reason for that remained unclear, just as the specific mechanism(s) of resistance in 1p/19q intact astrocytomas.

Here we describe the discovery of a direct anatomical connection between astrocytoma cells, with relevance for tumour functionality and resistance. Similar cell–cell connections by membrane tubes have been first described in *Drosophila* development[7]. They can play a role in the transport of organelles and proteins[8,9], spread of infectious particles[10], stem cell signalling[11], and functional cell–cell coupling[12–14]. Studied mostly *in vitro* so far, these tubes have received many names, including membrane nanotubes, tunnelling nanotubes, or cytonemes. However, the exact function(s) of membrane tube connections in mammalian tissues and in tumour biology remained unresolved[15].

Membrane tubes in glioma progression

To study the occurrence and dynamics of membrane tube protrusions in mammalian tumours, we followed gliomas growing in the mouse brain by *in vivo* multiphoton laser-scanning microscopy (MPLSM) down to a depth of 750 µm (ref. 16), for up to one year. After transplantation of patient-derived glioblastoma cell lines ($n = 6$) that were kept under serum-free, stem-like conditions[17] (GBMSCs; non-codeleted for 1p/19q, and *IDH* wild-type; Extended Data Fig. 1a–k), many tumour cells formed ultra-long cellular protrusions.

[1]Neurology Clinic and National Center for Tumor Diseases, University Hospital Heidelberg, INF 400, 69120 Heidelberg, Germany. [2]Clinical Cooperation Unit Neurooncology, German Cancer Consortium (DKTK), German Cancer Research Center (DKFZ), 69120 Heidelberg, Germany. [3]Department of Neuropathology, Institute of Pathology, Ruprecht-Karls University Heidelberg, INF 224, 69120 Heidelberg, Germany. [4]Clinical Cooperation Unit Neuropathology, German Cancer Consortium (DKTK), German Cancer Research Center (DKFZ), INF 224, 69120 Heidelberg, Germany. [5]Department of Functional Neuroanatomy, Institute of Anatomy and Cell Biology, Heidelberg University, INF 307, 69120 Heidelberg, Germany. [6]Department of Diagnostic and Interventional Neuroradiology, Klinikum rechts der Isar der Technischen Universität München, 81675 Munich, Germany. [7]Neurosurgery Clinic, University Hospital Heidelberg, INF 400, 69120 Heidelberg, Germany. [8]Department of Neuroradiology, University Hospital Heidelberg, INF 400, 69120 Heidelberg, Germany. [9]Department of Neurophysiology, Institute of Physiology, University of Würzburg, 97070 Würzburg, Germany. [10]Department of Medical Physics, German Cancer Research Center (DKFZ), 69120 Heidelberg, Germany. [11]Institute of Cellular Neurosciences, Medical Faculty, University of Bonn, Sigmund-Freud-Strasse 25, 53105 Bonn, Germany. [12]Light Microscopy Facility, German Cancer Research Center (DKFZ), 69120 Heidelberg, Germany. [13]Department of Translational Immunology, German Cancer Research Center (DKFZ), 69120 Heidelberg, Germany. [14]Department of Biomedicine, University of Bergen, Jonas Lies vei 91, 5009 Bergen, Norway. [15]Institute of Neurology, Medical University of Vienna, Vienna, Austria; Comprehensive Cancer Center, CNS Unit, Medical University of Vienna, 1090 Vienna, Austria. [16]Tools For Bio-Imaging, Max-Planck-Institute of Neurobiology, 82152 Martinsried, Germany. [17]Institute of Physiology II, Eberhard Karls University of Tübingen, 72074 Tübingen, Germany. [18]Department of Medicine I, Medical University of Vienna, Vienna, Austria; Comprehensive Cancer Center, CNS Unit, Medical University of Vienna, 1090 Vienna, Austria. [19]Hotchkiss Brain Institute, Faculty of Medicine, University of Calgary, Calgary, Alberta T2N 4N1, Canada. [20]Department of Cell Biology and Anatomy, Faculty of Medicine, University of Calgary, Calgary, Alberta T2N 4Z6, Canada. [21]Clark Smith Brain Tumor Research Centre, Southern Alberta Cancer Research Institute, Faculty of Medicine, University of Calgary, Calgary, Alberta, T2N 4N1, Canada. [22]Helmholtz Young Investigator Group, Normal and Neoplastic CNS Stem Cells, DKFZ-ZMBH Alliance, German Cancer Research Center (DKFZ), INF 280, 69120 Heidelberg, Germany. [23]Clinical Cooperation Unit Neuroimmunology and Brain Tumor Immunology, German Cancer Consortium (DKTK), German Cancer Research Center (DKFZ), 69120 Heidelberg, Germany. [24]CCU Molecular and Radiation Oncology, German Cancer Research Center (DKFZ), INF 280, 69120 Heidelberg, Germany. [25]Department of Radiation Oncology, University Hospital Heidelberg, 69120 Heidelberg, Germany.
*These authors contributed equally to this work.

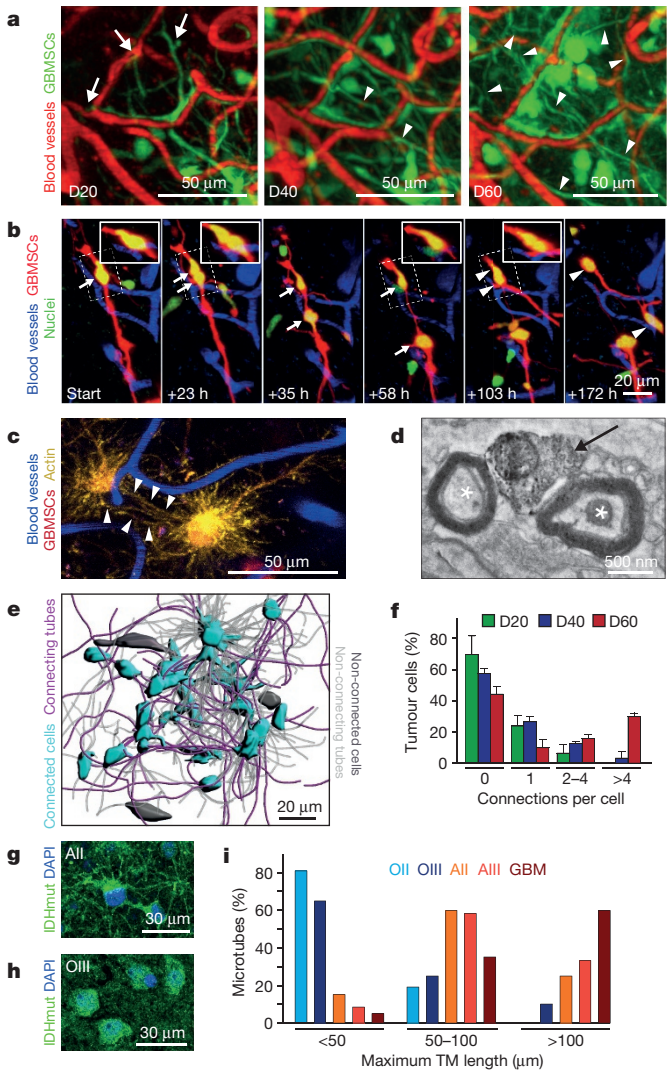

Figure 1 | Distinct membrane microtubes of brain tumour cells. **a**, *In vivo* MPLSM maximum intensity projections (MIPs) of S24 GBMSCs growing in the mouse brain over 60 days (D). Arrows, thin cellular protrusions extending into the normal brain; arrowheads, long intratumoral protrusions. **b**, Travel of nuclei (arrows, arrowheads) after nuclear division (at 23 and 103 h) in cellular protrusions of S24 GBMSCs. 3D images. **c**, Protrusions are actin-rich, and interconnect single tumour cells (arrowheads, S24 Lifeact-YFP, MIP). **d**, Scanning electron microscopy (SEM) image of a S24 GBMSC membrane microtube (arrow, identified by GFP photo-oxidation) in the mouse brain. Asterisks, axons. **e**, 3D rendering (*z* dimension 90 µm) of membrane microtubes interconnecting single S24 GBMSCs. Intercellular (connecting) and non-connecting tubes, and connected and unconnected tumour cells are shown colour-coded. **f**, Number of membrane microtubes per S24 tumour cell that connect this cell to another tumour cell ($n = 141–437$ cells in $n = 3$ mice). **g**, **h**, Representative confocal *IDH1R132H* mutation-specific immunofluorescence images of a human astrocytoma grade II (AII, **g**) and oligodendroglioma grade III (OIII, **h**). **i**, Maximum length of $IDH1^{R132H}$-positive microtubular structures in human oligodendrogliomas (O, 1p/19q codeleted) grade II, III; and astrocytomas (A, 1p/19q non-codeleted) grade II, III and IV (glioblastoma, GBM); $n = 20–24$ patients per tumour entity, $n = 105$ total. **a**–**c** and **e**–**f**, *in vivo* MPLSM. Error bars show s.d.

These protrusions infiltrated the normal brain at the invasive front (Fig. 1a), where astrocytoma cells extended and retracted them in a scanning mode (Supplementary Video 1). Protrusion tips were highly dynamic (Extended Data Fig. 1l), similar to neuronal growth cones during development[18]. When tumours progressed, the number of cellular protrusions increased further, some exceeding 500 µm in length (Extended Data Fig. 2a). The resulting membrane tubes where used as tracks for travel of cell nuclei, for example, after mitosis (Fig. 1b; speed of travelling nuclei: 66.42 ± 36.25 µm per day, $n = 16$ nuclei in $n = 6$ mice.). These data suggest that membrane tube formation is a novel means of tumour dissemination, adding to the known strategies[19].

All membrane tubes were actin-rich (Fig. 1c), which is also typical for most membrane nanotubes[8]. Moreover, live imaging and immunohistochemistry revealed that they were indeed enclosed by a continuous cell membrane, and positive for myosin IIa, microtubules, and protein disulphide isomerase; partly positive for β-catenin, β-parvin, and the astrocytic marker GFAP; but largely negative for N-cadherin, myosin X, and the neuronal marker β-tubulin III (Extended Data Fig. 2b, c). Together, these data indicate that these membrane tubes have a unique composition and a potent motility machinery. Dendritic arborization was frequent, with more dynamic thin membrane tubes originating from more stable, thicker ones (Fig. 1c, Extended Data Fig. 3a, b). To allow ultrastructural analysis of these thin tumour cell-derived tubes in the mouse brain by electron microscopy, photo-oxidation of brain sections was performed. This resulted in dark precipitates within the green fluorescent protein (GFP)-expressing astrocytoma cell tubes (Extended Data Fig. 3c). Serial-section scanning electron microscopy (3D SEM) revealed that the cell membrane-enclosed tubes had a mean cross-sectional area of 1.57 ± 0.33 µm^2 ($n = 6$, Extended Data Fig. 3d), and contained mitochondria and microvesicles (Fig. 1d), suggesting that there is local ATP production and vesicle trafficking in the tubes. Interestingly, mitochondria travelled quickly in these tubes (Extended Data Fig. 3e). Furthermore, a relevant number of membrane microtubes were following axons in the brain (19.6% of $n = 51$; Fig. 1d, Extended Data Fig. 3f), which are known leading structures for tumour cell dissemination in astrocytomas[20].

In vivo imaging of membrane tube development over time revealed that an increasing number started at one and ended at another astrocytoma cell, creating a multicellular anatomical network (Fig. 1e, f; Supplementary Video 2a, b). Abundant intercellular membrane tubes were also found in a genetic astrocytoma model[21] (Extended Data Fig. 3g, Supplementary Video 2c). Intercellular membrane tubes were in part a result of cell division, with enduring stable contact of daughter cells over long distances (Fig. 1b), but also of mating of non-related astrocytoma cells (Extended Data Fig. 4a–g). A small proportion of membrane tube-bearing astrocytoma cells maintained quiescent for months, often in a perivascular niche that has been associated with glioma cell stemness[22] (Extended Data Fig. 4h, i).

The intercellular position of many astrocytoma membrane tubes, together with their high content of F-actin, is reminiscent of membrane nanotubes[15]; however, the membrane nanotubes reported so far had a width of below 1 µm; a length of usually tens, rarely a few hundreds of µm; and documented life time of less than 60 min. These differences led us to propose the new term "tumour microtubes", or TMs, for the discovered ultra-long, long-lived, and thicker membrane extensions of astrocytoma cells.

TMs characterize human astrocytomas

To investigate whether TMs are also characteristic for human brain tumours, we stained resected WHO grade II–IV gliomas with $IDH1^{R132H}$ mutations using a mutation-specific antibody[23]. This allowed us to unambiguously detect tumour-cell-derived membrane tubes in the filament-rich brain parenchyma. Like in the astrocytoma mouse models, TMs were abundant in patient tissue (Fig. 1g): 63% of astrocytoma cells had intercellular TMs ($n = 196$ cells in 100 µm thick sections of $n = 8$ WHO grade II–III tumours without 1p/19q codeletion; Supplementary Video 3). In contrast, only 0.7% of oligodendroglioma cells in human tumour samples had intercellular TMs (Fig. 1h; $n = 150$ cells from $n = 3$ oligodendrogliomas with 1p/19q codeletion), and TMs were also rare in patient-derived oligodendroglioma cells that formed tumours in mice (Extended Data Fig. 5a, b). Further analysis of 105 human gliomas revealed that TM formation was highly influenced by tumour type and grade, with a marked positive correlation of TM

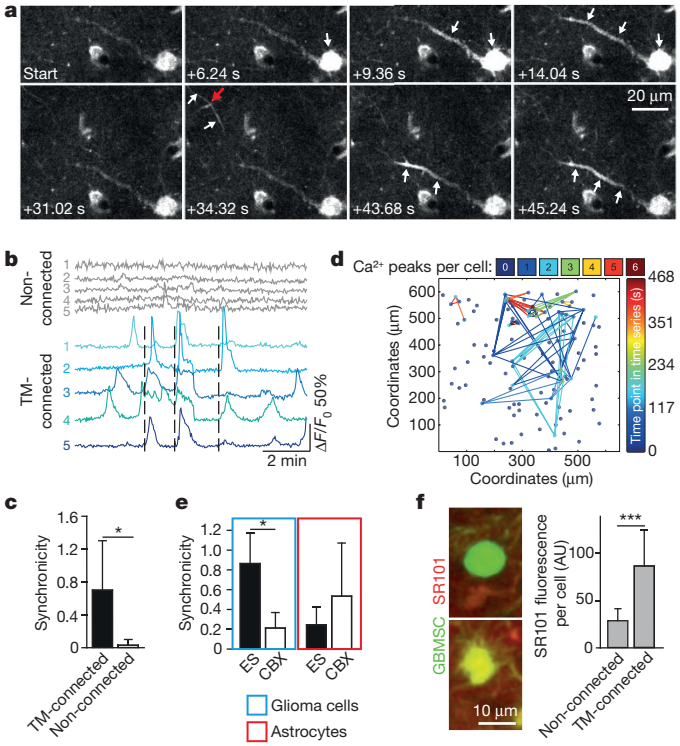

Figure 2 | TM-connections allow communication in multicellular networks. a, Time-lapse image of calcium waves (Rhod2-AM) travelling along TMs of GBMSCs (bidirectional; arrows). Red arrow, crossing of two TMs, with simultaneous calcium peak. **b**, Calcium transients ($\Delta F/F_0$, Rhod-2AM) of non-connected GMBSCs (grey) versus TM-connected cells (blue); broken lines mark synchronous calcium transients. **c**, Synchronicity (see Methods section) of calcium peaks in GBMSCs, shown for TM-connected versus non-TM-connected tumour cells ($n = 40$ versus 43 cells in $n = 3$ mice per condition; *t*-tests). **d**, Representative heat map of calcium transients between GBMSCs. **e**, Synchronicity of calcium peaks during brain superfusion with extracellular saline (ES, control) versus 100 µM carbenoxolone (CBX) in GBMSCs (blue box) and normal brain astrocytes (red box); $n = 3$ mice per group; *t*-tests. **f**, SR101 uptake in a non-TM-connected GBMSC (upper image) and a TM-connected one (lower image). Right, corresponding quantification (AU, arbitrary units); $n = 55$ cells in $n = 3$ mice per condition; Mann–Whitney test. All images and analyses, *in vivo* MPLSM. GBMSCs, S24 line. Error bars show s.d. $^*P < 0.05$, $^{***}P < 0.001$.

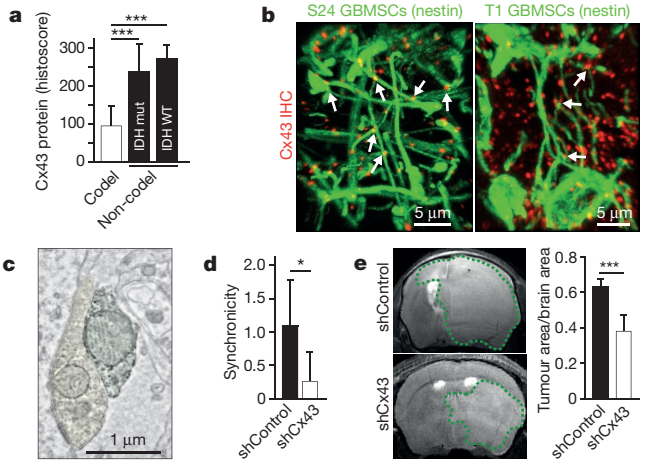

Figure 3 | Connexin 43 gap junctions connect TMs. a, Quantification of Cx43 protein expression detected by immunohistochemistry in 1p/19 non-codeleted (*IDH* wild-type and *IDH* mutated) versus codeleted human gliomas ($n = 8$ each, ANOVA, Tukey's post-hoc test). **b**, Nestin and Cx43 double-immunofluorescence in S24 and T1 GBMSC tumours (arrows: Cx43-positive TM-interconnections). **c**, SEM image of a direct membrane contact of 2 TMs in the mouse brain. **d**, Synchronicity of calcium peaks in S24 shControl versus shCx43 cells ($n = 3$ mice/condition; Mann–Whitney test). **e**, T2 MRI images of shControl versus shCx43 tumours, 72 days after implantation. Quantifications of $n = 6$ animals per group (*t*-test). **d**, *In vivo* MPLSM. Error bars show s.d. $^*P < 0.05$; $^{***}P < 0.001$.

length and unfavourable prognosis. For example, bona fide TMs of a minimum of 50 µm length in standard thin sections were detectable in only 19% of WHO grade II oligodendrogliomas, but 93% of WHO grade IV astrocytomas (= glioblastomas) (Fig. 1i). In astrocytomas, TMs were even detected in the contralateral brain hemisphere (Extended Data Fig. 5c), and also in *IDH* wild-type tumours (Extended Data Fig. 5d). The 1p/19q status better predicted TM occurrence than morphological glioma classification (Extended Data Fig. 5e–g).

A communicating network

Intercellular calcium waves (ICWs) can coordinate the activity of individual cells in multicellular networks, which includes astrocytes of the normal brain[24,25], neurons[26], and radial glia cells during central nervous system development[27]. We observed extensive and long-range ICWs, involving many astrocytoma cells in various tumour regions (Supplementary Video 4). ICWs were propagated along TMs in both directions (Fig. 2a, Extended Data Fig. 6a). Further analysis confirmed that ICWs, measured by synchronicity of calcium fluctuations, were largely restricted to astrocytoma cells with detectable TM connections (Fig. 2b, c; Extended Data Fig. 6b), allowing communication of individual cells in a reproducible pattern (Fig. 2b, d; Extended Data Fig. 6c, d).

For membrane nanotubes, intercellular connections have been reported *in vitro* to either be open ended[8], or separated by gap junctions[14], the latter as a prerequisite for ICW propagation[15]. Indeed, pharmacological gap junction blockade reduced the frequency (Extended Data Fig. 6e) and synchronicity (Fig. 2e) of TM-mediated ICWs in astrocytoma cells *in vivo*, but not in co-registered brain astrocytes of that tumour region. Inhibition of inositol triphosphate, which is gap-junction-permeable and the effector of gap-junction-mediated ICW propagation[26] also reduced ICWs between astrocytoma cells (Extended Data Fig. 6f).

The functional connection of single astrocytoma cells via TM-associated gap junctions was verified by rapid distribution of the gap junction-permeable dye sulforhodamine 101 (ref. 28) in the TM-connected cellular tumour cell network *in vivo* after local injection (Fig. 2f), which was inhibited by gap junction blockade (Extended Data Fig. 5g). Further experiments confirmed that another gap junction-permeable molecule was transferred between TM-connected cells (Extended Data Fig. 6h–j), while gap junction-impermeable large molecules were not (Extended Data Fig. 4c).

Connexin 43 connects TMs

To identify which of the known gap-junction-forming human connexins is involved in TM-mediated cell-to-cell communication in astrocytomas, we hypothesized that the deficiency of 1p/19q codeleted gliomas for intercellular TMs might also result in lower expression of the relevant TM-associated connexin(s). Analysis of 250 glioma samples of the TCGA data set revealed a list of differentially expressed genes between 1p/19q codeleted versus non-codeleted human tumours. Of the 20 connexins for which reads were mapped, only connexin 43 (also known as Cx43, GJA1) was differentially expressed, and found to be among the top 100 upregulated genes in 1p/19q non-codeleted tumours, both in *IDH* mutated and wild-type ones (Supplementary Table 1). This was confirmed in patient tumour tissue (Fig. 3a), and also in the primary glioma cell lines (Extended Data Fig. 6k). Confocal microscopy revealed punctate Cx43 immunoreactivity particularly at the TMs of astrocytoma cells (Fig. 3b), which was not seen for other connexins (Extended Data Fig. 6l). Remarkably, Cx43 immunoreactivity frequently located at the place where two different TMs crossed each

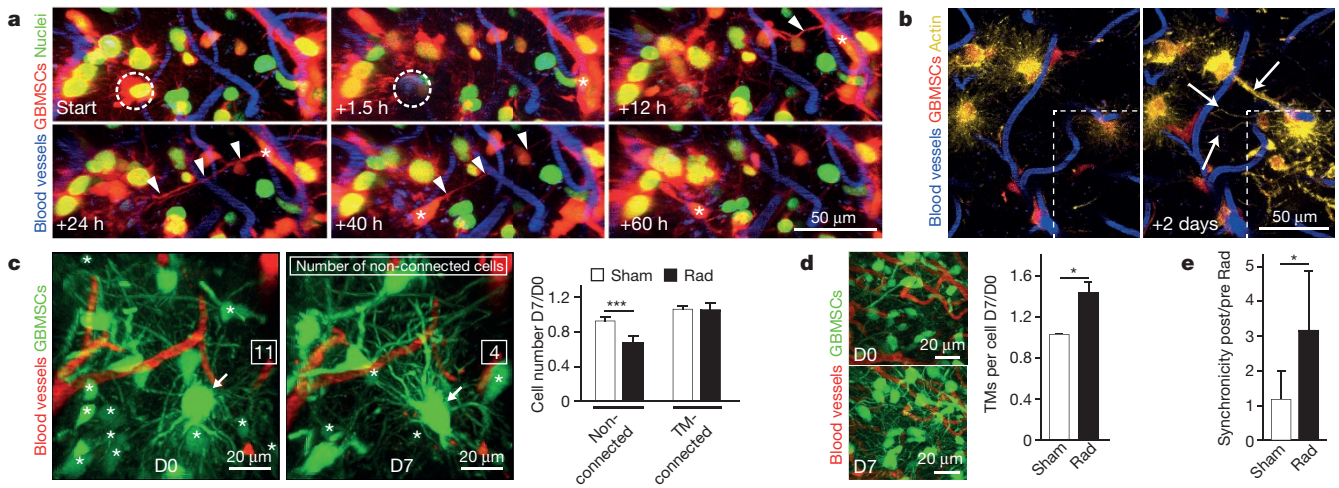

Figure 4 | TM-connected astrocytoma cell networks can repair themselves, and resist radiotherapy. a, Time series of exemplary 3D images (54 µm thickness) of a tumour region after laser-induced killing of a GMBSC (circle). Over time a TM (arrowheads) is extended, and a nucleus (asterisk) translocates via that TM to the place the killed cell had been located. **b**, Time course after laser-induced photodamage (dotted area), arrows: GBMSC TMs extending into the photodamaged region. MIP of 21 µm, $n = 3$ mice. **c**, GBMSC tumour microregions (3D images, 20 µm depth) before start of radiation (D0), and 7 days later (D7). Asterisks, non-TM-connected GBMSCs; arrow, one exemplary cell with many TMs. Graph, relative change of cellular subtypes under sham radiation (Sham), or treated with radiation at 3×7 Gy (Rad) ($n = 3$ mice per group, *t*-tests). **d**, Number of TMs per cell in these *t*umours (3D images left side, $n = 50$ cells per time point in $n = 3$ mice per group, Mann–Whitney test). **e**, Synchronicity of calcium transients after sham treatment or radiotherapy in individual GBMSC tumour regions (Fluo-4AM, $n = 3$ mice per group, Mann–Whitney test). All images, *in vivo* MPLSM. GBMSCs, S24 line. Error bars show s.d. $^*P < 0.05$, $^{***}P < 0.001$.

other (Fig. 3b). Contact sites of individual TMs with direct membrane–membrane contact were also detected with 3D SEM (Fig. 3c). Further analysis of our ICW data sets revealed that calcium waves can propagate via those crossings from one TM to another (Fig. 2a, red arrow).

To investigate the functional role of the Cx43 gap junction protein in astrocytoma progression, a stable short hairpin RNA knockdown of Cx43 was performed in GBMSCs. This significantly reduced the synchronicity of ICWs *in vivo* (Fig. 3d), and also the proportion of astrocytoma cells with multiple TMs at later time points (Extended Data Fig. 6m), which suggests a role for Cx43 gap-junction-mediated communication in long-term stabilization of TMs. In accordance with the proposed role of functional TMs for tumour progression, Cx43 deficiency resulted in reduced tumour size as observed by MRI (Fig. 3e) and improved survival (Extended Data Fig. 6n).

A self-repairing and resistant network

To investigate the role of TMs in damage repair *in vivo*, selective ablation of single GBMSCs was performed by applying a fatal laser dose to a fraction of their nuclear volume (1 µm^3). If the ablated cell was a prior member of the TM-connected network, new TMs were extended towards the dead cell, and within a few days a new nucleus advanced via those TMs to the location of the prior cell (Fig. 4a; $n = 8$ reconstitution events in 8 photodamaged tumour cells from $n = 3$ animals). If a non-TM-connected GBMSC was ablated, such repair mechanism was only infrequently observed (2/8 events in $n = 3$ animals; $P < 0.01$, Fisher's exact test). Photon damage to a larger volume consisting of 6–10 GBMSCs and normal brain parenchyma resulted in rapid extension of TMs of neighbouring GBMSCs into this area, followed by a marked increase in tumour cell density specifically in the damaged volume (Fig. 4b).

Next we investigated whether TM-connected tumour cell networks were also resistant against the cytotoxic effects of radiation therapy, a standard treatment of gliomas. While TM-connected cells were largely protected from cell death, unconnected tumour cells died in relevant numbers after radiotherapy (Fig. 4c, Extended Data Fig. 7a, b). Furthermore, TM-connected astrocytoma cells increased both their TM number (Fig. 4d) and their calcium communication (Fig. 4e, Extended Data Fig. 7c) as a reaction to radiotherapy. Concordantly, Cx43 knockdown reduced the radioprotective effect of TM interconnections, while non-TM-connected astrocytoma cells regressed like in control tumours (Extended Data Fig. 7d).

To explore potential mechanisms of TM-mediated protection from cytotoxicity, we measured basal intracellular calcium levels in astrocytoma cells before and during radiotherapy, using a ratiometric calcium indicator. Basal calcium levels were very homogeneous in non-irradiated cells, and also in TM-connected cells during radiotherapy, while unconnected cells developed a high variability of their intracellular calcium levels during irradiation (Extended Data Fig. 7e–h).

Drivers of TM formation

Next we sought to identify the crucial molecular pathways that drive the formation of TMs to better understand their nature, and to substantiate their role for tumour progression and resistance. For this purpose, we first analysed the *in silico* data set of 1p/19q non-codeleted versus codeleted human gliomas (Supplementary Table 1) by using Ingenuity Pathway Analysis. Here, biological functions that were prominently activated in 1p/19q non-codeleted astrocytomas included "cellular movement" and "cell-to-cell signalling and interaction", supporting the proposed function of TMs in these tumours (Extended Data Fig. 8a, b for *IDH* mutant astrocytomas; similar results for *IDH* wild-type astrocytomas, data not shown). Intriguingly, we found many canonical pathways involved in the outgrowth of neurites, and neurite-like membrane protrusions to be more activated in 1p/19q non-codeleted gliomas, including integrin[29], phospholipase C[30], Rho family GTPases[31], HMGB1[32], and also the prototypical neurotrophin/TRK signalling pathways[30] (Extended Data Fig. 8c; confirmed in *IDH* wild-type astrocytomas, data not shown). The latter was confirmed at the protein level in human gliomas, where the neurotrophins NGF (located on 1p) and NT-4 (19q) were downregulated in 1p/19q codeleted tumours, and also their respective membrane receptors TrkA and TrkB, which has been described before[33] (Extended Data Fig. 9a).

When considering these results and reviewing the literature for known downstream effectors particularly relevant for the formation of neurite-like membrane protrusions, the growth-associated protein GAP-43 came into focus. GAP-43 is highly expressed in axonal growth cones[34,35], induced by neurotrophin receptor signalling[36,37], and drives neuronal progenitor cell migration[38]. Remarkably, GAP-43

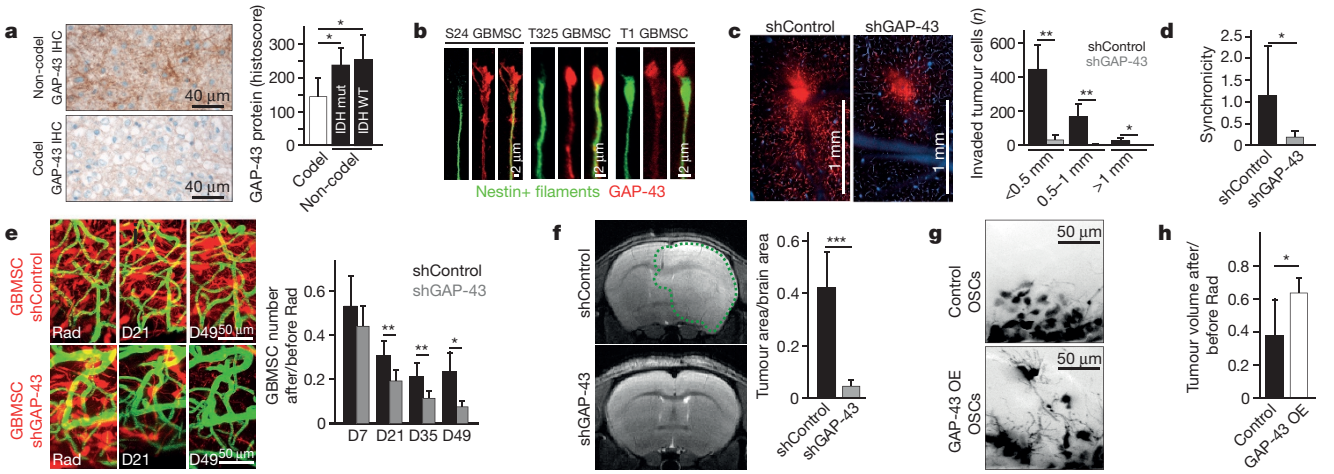

Figure 5 | GAP-43 is required for TM outgrowth and function. **a**, GAP-43 protein expression (immunohistochemistry) in 1p/19 non-codeleted (*IDH* wild-type and *IDH* mutated) versus codeleted gliomas ($n = 8$ each) (ANOVA on the ranks, Student–Newman–Keuls post hoc test). **b**, Immunocytological images of GAP-43 protein, with preferential GAP-43 localization at the tip of TMs. **c**, Single-plane images of control and shGAP-43 knockdown GBMSC S24 tumours; right, corresponding quantification ($n = 3$ mice per condition; Mann–Whitney tests). **d**, Synchronicity analysis of calcium peaks in S24 shControl versus shGAP-43 cells *in vivo* ($n = 3$ mice; Mann–Whitney test). **e**, Time course after irradiation of S24 shControl versus shGAP-43 tumours, corresponding quantifications ($n = 3$ mice per group; *t*-tests). **f**, MRI images of S24 shControl versus shGAP-43 tumours, 60 days after radiation (115 days after tumour implantation); right, quantifications of 5–6 animals per group (*t*-test). **g**, GAP-43 overexpression in BT088 oligodendroglial stem-like cell lines (OSCs) versus controls, 14 days after injection. **h**, Relative change of tumour volumes 21 days after radiotherapy in BT088 vector-control versus GAP-43 overexpression tumours ($n = 3$ mice per group; *t*-test). **c**–**e**, **g**, **h**, *In vivo* MPLSM. Error bars show s.d. $*P < 0.05$, $**P < 0.01$, $***P < 0.001$.

overexpression is sufficient for the outgrowth of membrane tubes in neuronal[39] and even in non-neuronal[40] cells. Indeed, GAP-43 was significantly higher expressed in 1p/19q non-codeleted human gliomas (Fig. 5a) and primary stem-like cell lines (Extended Data Fig. 9b, c) when compared with 1p/19q codeleted ones. Of note, GAP-43 preferentially localized to the cone-like and nestin-negative tips of sprouting TMs (Fig. 5b), similar to its known enrichment in the nerve growth cone[35].

To interfere with TM formation during astrocytoma progression, we engineered GBMSCs with a genetic knockdown of GAP-43. While *in vitro* viability of these cells was not affected (data not shown), their TMs *in vivo* were structurally abnormal, with reduced branching (Extended Data Fig. 9d). This was associated with an impaired dissemination of tumour cells (Fig. 5c, Extended Data Fig. 9e), resulting from both their decreased mean invasion speed (Extended Data Fig. 9f) and proliferation capacity (Extended Data Fig. 9g) in the mouse brain. Importantly, intercellular TM connections (Extended Data Fig. 9h) and ICWs (Fig. 5d) were reduced in GAP-43 deficient tumours, which was accompanied by a selective reduction of Cx43 gap junction protein expression (Extended Data Fig. 9i). These deficiencies in TM-mediated features of tumour progression lead to a marked reduction of tumour size in the mouse brain (Extended Data Fig. 9j), and to an improved survival of the animals (Extended Data Fig. 9k). When radiotherapy was applied, GAP-43 deficiency resulted in an increased regression of tumour cells, as revealed by repetitive *in vivo* MPLSM (Fig. 5e). This was confirmed by MRIs 60 days after radiation, where no relevant tumour-derived signal changes were detectable in shGap43 tumour bearing animals, while control tumours were large, causing neurological symptoms in mice (Fig. 5f). Histological analysis at this time point confirmed only small remnants of proliferation-deficient tumour cells in GAP-43 knockdown tumours (Extended Data Fig. 9l).

Finally, we overexpressed the GAP-43 protein in 1p/19q codeleted primary oligodendroglioma cells, to achieve protein levels comparable to the 1p/19q non-codeleted GBMSC lines (Extended Data Fig. 9m). This lead to a morphological shift to a TM-rich, thus astrocytoma-like phenotype of GAP-43 overexpressing oligodendroglioma cells (Fig. 5g, Extended Data Fig. 9n, o). Remarkably, the induction of TM formation in these tumours resulted in an increase in tumour cell invasion into the brain (Fig. 5g, Extended Data Fig. 9p), and also in an increase in radioresistance (Fig. 5h); both were comparably low in control oligodendrogliomas.

Conclusions

The ability to interconnect via ultra-long and highly functional TMs is an important mechanism of progression and resistance in astrocytomas, and depends on molecular pathways that are active when 1p/19q is intact. The resulting multicellular network is able to communicate via Cx43 gap junction connections. Multiple functions have been reported previously for different connexins in glioma pathology[41,42]. This includes Cx43, which is also highly expressed in non-malignant astrocytes, connecting them to functional and resistant[43] cellular networks. Here we provide one possible mechanism for this resistance: maintenance of calcium homeostasis by network integration. Since increases of intracellular calcium levels are required for radiotherapy-induced cytotoxicity[44], and even small calcium increases are involved in intrinsic apoptotic cell death in glioma cells[45], one can assume that intercellular TMs can serve as a means for an individual tumour cell to distribute critical elevations of small molecules like calcium within the larger network, achieving nonlethal levels.

The data presented here support the notion that tumours are complex organs, which has so far been attributed to the supportive contribution of non-malignant cell types[46], including neurons in brain tumours[47]. Our study adds to this concept by demonstrating that single cancer cells within one tumour communicate and cooperate with each other in a complex but ordered manner that is by itself reminiscent of a functional organ. It has become clear that tumours can hijack programs that are part of normal tissue development[48]. The key finding of this study is that TMs, which are generated by GAP-43 just as axons are in neurons, allow efficient tumour progression, network communication, and resistance to adverse events (Extended Data Fig. 10). Thus we anticipate that pharmacological targeting of TM formation and function will open new therapeutical avenues for treatment-resistant brain tumours.

Online Content Methods, along with any additional Extended Data display items and Source Data, are available in the online version of the paper; references unique to these sections appear only in the online paper.

Received 15 December 2014; accepted 9 October 2015.
Published online 4 November; corrected online 2 December 2015 (see full-text HTML version for details).

1. Cuddapah, V. A., Robel, S., Watkins, S. & Sontheimer, H. A neurocentric perspective on glioma invasion. *Nature Rev. Neurosci.* **15,** 455–465 (2014).
2. The Cancer Genome Atlas Research Network. Comprehensive, integrative genomic analysis of diffuse lower-grade gliomas. *N. Engl. J. Med.* **372,** 2481–2498 (2015).
3. Eckel-Passow, J. E. *et al.* Glioma groups based on 1p/19q, *IDH*, and *TERT* promoter mutations in tumors. *N. Engl. J. Med.* **372,** 2499–2508 (2015).
4. Wiestler, B. *et al.* Integrated DNA methylation and copy-number profiling identify three clinically and biologically relevant groups of anaplastic glioma. *Acta Neuropathol.* **128,** 561–571 (2014).
5. van den Bent, M. J. *et al.* Adjuvant procarbazine, lomustine, and vincristine chemotherapy in newly diagnosed anaplastic oligodendroglioma: long-term follow-up of EORTC brain tumor group study 26951. *J. Clin. Oncol.* **31,** 344–350 (2013).
6. Cairncross, G. *et al.* Phase III trial of chemoradiotherapy for anaplastic oligodendroglioma: long-term results of RTOG 9402. *J. Clin. Oncol.* **31,** 337–343 (2013).
7. Ramírez-Weber, F. A. & Kornberg, T. B. Cytonemes: cellular processes that project to the principal signaling center in *Drosophila* imaginal discs. *Cell* **97,** 599–607 (1999).
8. Rustom, A., Saffrich, R., Markovic, I., Walther, P. & Gerdes, H. H. Nanotubular highways for intercellular organelle transport. *Science* **303,** 1007–1010 (2004).
9. Lou, E. *et al.* Tunneling nanotubes provide a unique conduit for intercellular transfer of cellular contents in human malignant pleural mesothelioma. *PLoS One* **7,** e33093 (2012).
10. Sowinski, S. *et al.* Membrane nanotubes physically connect T cells over long distances presenting a novel route for HIV-1 transmission. *Nature Cell Biol.* **10,** 211–219 (2008).
11. Inaba, M., Buszczak, M. & Yamashita, Y. M. Nanotubes mediate niche-stem-cell signalling in the *Drosophila* testis. *Nature* **523,** 329–332 (2015).
12. Hsiung, F., Ramirez-Weber, F. A., Iwaki, D. D. & Kornberg, T. B. Dependence of *Drosophila* wing imaginal disc cytonemes on Decapentaplegic. *Nature* **437,** 560–563 (2005).
13. Smith, I. F., Shuai, J. & Parker, I. Active generation and propagation of Ca^{2+} signals within tunneling membrane nanotubes. *Biophys. J.* **100,** L37–L39 (2011).
14. Wang, X., Veruki, M. L., Bukoreshtliev, N. V., Hartveit, E. & Gerdes, H. H. Animal cells connected by nanotubes can be electrically coupled through interposed gap-junction channels. *Proc. Natl Acad. Sci. USA* **107,** 17194–17199 (2010).
15. Sherer, N. M. Long-distance relationships: do membrane nanotubes regulate cell-cell communication and disease progression? *Mol. Biol. Cell* **24,** 1095–1098 (2013).
16. Kienast, Y. *et al.* Real-time imaging reveals the single steps of brain metastasis formation. *Nature Med.* **16,** 116–122 (2010).
17. Lee, J. *et al.* Tumor stem cells derived from glioblastomas cultured in bFGF and EGF more closely mirror the phenotype and genotype of primary tumors than do serum-cultured cell lines. *Cancer Cell* **9,** 391–403 (2006).
18. Lowery, L. A. & Van Vactor, D. The trip of the tip: understanding the growth cone machinery. *Nature Rev. Mol. Cell Biol.* **10,** 332–343 (2009).
19. Friedl, P. & Alexander, S. Cancer invasion and the microenvironment: plasticity and reciprocity. *Cell* **147,** 992–1009 (2011).
20. Scherer, H. J. The forms of growth in gliomas and their practical significance. *Brain* **63,** 1–35 (1940).
21. Zhu, Z. *et al.* Targeting self-renewal in high-grade brain tumors leads to loss of brain tumor stem cells and prolonged survival. *Cell Stem Cell* **15,** 185–198 (2014).
22. Calabrese, C. *et al.* A perivascular niche for brain tumor stem cells. *Cancer Cell* **11,** 69–82 (2007).
23. Capper, D., Zentgraf, H., Balss, J., Hartmann, C. & von Deimling, A. Monoclonal antibody specific for *IDH1* R132H mutation. *Acta Neuropathol.* **118,** 599–601 (2009).
24. Kuchibhotla, K. V., Lattarulo, C. R., Hyman, B. T. & Bacskai, B. J. Synchronous hyperactivity and intercellular calcium waves in astrocytes in Alzheimer mice. *Science* **323,** 1211–1215 (2009).
25. Cornell-Bell, A. H., Finkbeiner, S. M., Cooper, M. S. & Smith, S. J. Glutamate induces calcium waves in cultured astrocytes: long-range glial signaling. *Science* **247,** 470–473 (1990).
26. Leybaert, L. & Sanderson, M. J. Intercellular Ca^{2+} waves: mechanisms and function. *Physiol. Rev.* **92,** 1359–1392 (2012).
27. Weissman, T. A., Riquelme, P. A., Ivic, L., Flint, A. C. & Kriegstein, A. R. Calcium waves propagate through radial glial cells and modulate proliferation in the developing neocortex. *Neuron* **43,** 647–661 (2004).
28. Nimmerjahn, A., Kirchhoff, F., Kerr, J. N. & Helmchen, F. Sulforhodamine 101 as a specific marker of astroglia in the neocortex *in vivo*. *Nature Methods* **1,** 31–37 (2004).
29. Tomaselli, K. J., Neugebauer, K. M., Bixby, J. L., Lilien, J. & Reichardt, L. F. N-cadherin and integrins: two receptor systems that mediate neuronal process outgrowth on astrocyte surfaces. *Neuron* **1,** 33–43 (1988).
30. Stephens, R. M. *et al.* Trk receptors use redundant signal transduction pathways involving SHC and PLC-γ1 to mediate NGF responses. *Neuron* **12,** 691–705 (1994).
31. Kozma, R., Sarner, S., Ahmed, S. & Lim, L. Rho family GTPases and neuronal growth cone remodelling: relationship between increased complexity induced by Cdc42Hs, Rac1, and acetylcholine and collapse induced by RhoA and lysophosphatidic acid. *Mol. Cell. Biol.* **17,** 1201–1211 (1997).
32. Fang, P., Schachner, M. & Shen, Y. Q. HMGB1 in development and diseases of the central nervous system. *Mol. Neurobiol.* **45,** 499–506 (2012).
33. Wang, Y. *et al.* Trk A, B, and C are commonly expressed in human astrocytes and astrocytic gliomas but not by human oligodendrocytes and oligodendroglioma. *Acta Neuropathol.* **96,** 357–364 (1998).
34. Goslin, K., Schreyer, D. J. & Skene, J. H. & Banker, G. Development of neuronal polarity: GAP-43 distinguishes axonal from dendritic growth cones. *Nature* **336,** 672–674 (1988).
35. Skene, J. H. *et al.* A protein induced during nerve growth (GAP-43) is a major component of growth-cone membranes. *Science* **233,** 783–786 (1986).
36. Lavenius, E., Gestblom, C., Johansson, I., Nånberg, E. & Påhlman, S. Transfection of TRK-A into human neuroblastoma cells restores their ability to differentiate in response to nerve growth factor. *Cell Growth Differ.* **6,** 727–736 (1995).
37. Koponen, E., Lakso, M. & Castrén, E. Overexpression of the full-length neurotrophin receptor trkB regulates the expression of plasticity-related genes in mouse brain. *Brain Res. Mol. Brain Res.* **130,** 81–94 (2004).
38. Haag, D. *et al.* Nos2 inactivation promotes the development of medulloblastoma in *Ptch1*$^{+/-}$ mice by deregulation of Gap43-dependent granule cell precursor migration. *PLoS Genet.* **8,** e1002572 (2012).
39. Aigner, L. *et al.* Overexpression of the neural growth-associated protein GAP-43 induces nerve sprouting in the adult nervous system of transgenic mice. *Cell* **83,** 269–278 (1995).
40. Zuber, M. X., Goodman, D. W., Karns, L. R. & Fishman, M. C. The neuronal growth-associated protein GAP-43 induces filopodia in non-neuronal cells. *Science* **244,** 1193–1195 (1989).
41. Sin, W. C., Crespin, S. & Mesnil, M. Opposing roles of connexin43 in glioma progression. *Biochim. Biophys. Acta* **1818,** 2058–2067 (2012).
42. Hitomi, M. *et al.* Differential connexin function enhances self-renewal in glioblastoma. *Cell Reports* **11,** 1031–1042 (2015).
43. Le, H. T. *et al.* Gap junction intercellular communication mediated by connexin43 in astrocytes is essential for their resistance to oxidative stress. *J. Biol. Chem.* **289,** 1345–1354 (2014).
44. Tombal, B., Denmeade, S. R., Gillis, J. M. & Isaacs, J. T. A supramicromolar elevation of intracellular free calcium ($[Ca^{2+}]_i$) is consistently required to induce the execution phase of apoptosis. *Cell Death Differ.* **9,** 561–573 (2002).
45. McFerrin, M. B., Turner, K. L., Cuddapah, V. A. & Sontheimer, H. Differential role of IK and BK potassium channels as mediators of intrinsic and extrinsic apoptotic cell death. *Am. J. Physiol. Cell Physiol.* **303,** C1070–C1078 (2012).
46. Hanahan, D. & Weinberg, R. A. Hallmarks of cancer: the next generation. *Cell* **144,** 646–674 (2011).
47. Venkatesh, H. S. *et al.* Neuronal activity promotes glioma growth through neuroligin-3 secretion. *Cell* **161,** 803–816 (2015).
48. Egeblad, M., Nakasone, E. S. & Werb, Z. Tumors as organs: complex tissues that interface with the entire organism. *Dev. Cell* **18,** 884–901 (2010).

Supplementary Information is available in the online version of the paper.

Acknowledgements We thank C. Ruiz de Almodovar and H.-H. Gerdes for discussions and comments; P. Rübman, B. Kast, A. Habel, A. Tietz-Dalfuβ and M. Fischer for technical assistance; R. Hermann for help with vibratome slices; G. Eisele for providing the WJ cell line; P. Friedl for the Lifeact-YFP-construct and the *IDH1*^{R132H} thick section staining protocol; H. Glimm for the pCCL.PPT.SFFV.MCS.IRES.eGFP.WPRE-vector backbone; and M. Splinter, M. Brand, C. Lang for help with radiation experiments. This work was funded by grants from the German Research Foundation (DFG, WI 1930/5-1 (F.W.) and Major Equipment Grant INST 114089/26-1 FUGG (F.W., W.W.)), an intramural grant from the DKFZ to F.W. and H.L., Heinrich F. C. Behr-Stipend to S. Weil. F.S. is a fellow of the Medical Faculty Heidelberg PostDoc-Program. The results published here are in part based upon data generated by the TCGA Research Network: http://cancergenome.nih.gov/.

Author Contributions F.W., M.O. and W.W. were responsible for experimental design, data interpretation, and writing of the manuscript. M.O., E.J., S. Weil and Y.L. performed MPLSM experiments. F.S. and A.v.D. performed stainings and analyses of human glioma tissues. M.O., M.G., E.J., S. Weil performed cell culture and cranial window implantations. G.S. was responsible for quantification and analysis of the calcium data. T.K., H.H., V.V. provided electron microscopy data and corresponding analyses. B.W. performed the TCGA data analysis. F.T.K. and S.H. collected MRI data. J.B. and T.S., M.R. and K.K.J. performed cell culture experiments, S.P. and D.L. established and characterized cell lines. A.S.B., L.H. and M. Preusser conducted histological experiments. V.H. and C.S. constructed the rrl-CAG-IGC3 vector. O. Griesbeck, G.K. and O. Garaschuk constructed the Twitch-3 vector, and interpreted the calcium imaging data. M.S. performed analyses of thick human tumour slices. M. Pauli conducted electroporation experiments. P.H. and P.E.H. were responsible for radiation. D.K. performed analysis of image data and confocal image acquisition. M. Platten performed data interpretation. M.J. performed FACS sorting. H.M. and S. Weiss provided cell lines and interpreted data. H.L. provided the syngeneic tumour model.

Author Information Reprints and permissions information is available at www.nature.com/reprints. The authors declare no competing financial interests. Readers are welcome to comment on the online version of the paper. Correspondence and requests for materials should be addressed to F.W. (frank.winkler@med.uni-heidelberg.de).

METHODS

Animals, and surgical procedures. 8–10 weeks old male NMRI nude mice were used for all studies with human primary brain tumour cells. As a syngeneic astrocytoma mouse model we used Nestin-Tv-a;Tlx-GFP mice in combination with RCAS-PDGFB/AKT vectors[21]. All animal procedures were performed in accordance with the institutional laboratory animal research guidelines after approval of the Regierungspräsidium Karlsruhe, Germany (governmental authority). All efforts were made to minimize animal suffering and to reduce the number of animals used. Mice were clinically scored and if they showed marked neurological symptoms or weight loss of >20%, experiments were terminated. In none of the experiments these limits were exceeded. No maximum tumour size was defined for the invasive brain tumour models.

Cranial window implantation in mice was done in a modification of what has been previously described[49], including a custom-made titanium ring for painless head fixation during imaging.

2–3 weeks after cranial window implantation, 30,000 tumour cells were stereotactically injected into the mouse brain at a depth of 500 µm. For survival experiments we injected 50,000 tumour cells. In a subgroup of mice, a short plastic tube was glued under the glass, with one end inside and one outside, which allowed topical application of different substances under the window without the need to re-open it.

For intratumoral microinjection of sulforhodamine 101 (SR101, Molecular Probes, S-359), 50 nl of 100 µM SR101 (with or without 100 µM CBX, Sigma-Aldrich, C4790) were injected with a very thin glass pipette into tumour regions of similar cellular densities, >90 days after tumour injection.

Radiation treatment. Established tumours were irradiated with 7 Gy on three consecutive days (total dose 21 Gy) in regions matching in tumour cell density using a 6 MV linear accelerator with a 6 mm collimator (adjusted to the window size) at a dose rate of 3 Gy min^{-1} (Artiste, Siemens), or no radiation was applied (sham radiation), at day 60 (±10 days) after tumour implantation. For MRI studies, a total brain radiation with the same dose and a field size of 17 mm × 250 mm (allowing the irradiation of several mice) was used. The used radiation schedule is in the range of the commonly prescribed 60 Gy in 2 Gy fractions for malignant glioma patients, assuming an α/β of ~ 10 in the linear quadratic model and taking into account the radiation time of 3 days.

***In vivo* multiphoton laser scanning microscopy (MPLSM).** MPLSM imaging was done with a Zeiss 7MP microscope (Zeiss) equipped with a Coherent Chameleon UltraII laser (Coherent). The following wavelengths were used for excitation: 750 nm (dsRed, FITC-dextrane, tdTomato), 840 nm (Fluo-4AM), 850 nm (GFP, TRITC-dextrane, Rhod-2AM), 860 nm (CFP, for Förster Resonance Energy Transfer (FRET) imaging) and 950 nm (tdTomato, YFP). Appropriate filter sets (band pass 500–550 nm/band pass 575–610 nm and band pass 460–500 nm/band pass 525–560 nm (for FRET)) were used. Standard settings for imaging were gains between 650 and 750 nm (depending on the depth, the fluorescence intensity of the fluorophore and the window quality), and a *z*-interval of 3 µm. Laser power was tuned as low as possible.

The body temperature of mice was kept constant using a rectal thermometer and a heating pad. Isoflurane concentration (in 100% O_2) was chosen as low as possible (0.5–1.5%) to avoid interference with the calcium communication between astrocytoma cells. Fluorescent dextranes (FITC (2M MW)- or TRITC (500.000 MW)-conjugated, 10 mg ml^{-1}, Sigma) were injected intravenously to obtain angiograms.

For *in vivo* ablation of single astrocytoma cells, only the volume of the GFP-labelled cell nucleus was exposed to continuous scanning with a high power laser beam until disintegration of the nucleus became visible. To investigate the reaction of TMs after the photodamage of a wider brain region, a larger volume ($0.5–1 \times 10^6$ μm^3) was scanned repetitively for approximately 8 min with high power, resulting in a total photon dose that was >50 times higher than during "diagnostic" imaging.

***In vivo* calcium imaging with MPLSM.** The following small molecule calcium indicators were applied to the brain surface for 45 min: for GFP-transfected tumour cells, 2 mM Rhod-2AM (Life Technologies, R-1244); for RFP-transfected, 2 mM Fluo-4AM (Life Technologies, F-14201). Pharmacological gap junction inhibition was achieved by superfusion with the inhibitor CBX (100 µM; control substance: extracellular saline; $n = 3$ mice per group). Other superfused substances were suramin (100 µM, ATP antagonist) and 2-aminoethoxydiphenyl borate (2-APB, 100 µM, inhibitor of inositol triphosphate receptors). Two genetically encoded calcium indicators were lentivirally transduced to GBMSCs: the Lck-GCaMP3 sensor in the rrl-CAG-lGC3 vector (CAG promoter to control expression of DsRed and the Ca^{2+} sensor that monitors near-membrane changes in $[Ca^{2+}]_i$[50]). The ratiometric calcium sensor Twitch-3 was used to determine intracellular calcium concentrations by FRET as previously described[51].

MRI studies. MRI images were obtained at day 72 after tumour implantation for non–irradiated animals, and at day 115 for irradiated mice (60 days after radiotherapy; time points were chosen when first control animals developed neurological symptoms and/or lost 20% weight, and had to be euthanized). All scans were performed on a 9.4 T horizontal bore MR scanner (BioSpec 94/20 USR, Bruker BioSpin GmbH) with a four channel phased array surface coil. A T2-weighted rapid acquisition with refocused echoes (RARE) sequence was acquired to determine tumour volume.

Cell lines and cell culture experiments. Tumour cell lines derived from resected glioblastomas were cultivated in DMEM-F12 under serum-free non-adherent, 'stem-like' conditions, including B27 supplement (12587-010, Gibco), insulin, heparin, epidermal growth factor and fibroblast growth factor[17,52] (GBMSCs: P3, S24, T1, T269, T325, WJ). These 6 GBMSC lines were selected because they were capable of growing to tumours in mouse brains; all were non-codeleted for 1p/19q, and *IDH* wild-type. Two oligodendroglioma cell lines harbouring the typical 1p/19q codeletion (BT088 and BT054) were kept under the same cell culture conditions[53]. Of note, BT054 is $IDH1^{R132H}$ mutated, while BT088 has lost the heterozygous $IDH1^{R132H}$ mutation of the patient tumour it was derived from, but still maintains its GCIMP phenotype (data not shown). Typical genetic changes of glioblastoma were confirmed for S24 using comparative genomic hybridization (CGH, see Extended Data Fig. 1i); the T1, T269, T325 and WJ lines had been characterized before[52], as well as the P3 line[54]. Cells were regularly checked for mycoplasma infections and authenticity (species control).

Tumour cells were transduced with lentiviral vectors for multicolour imaging. For cytosolic GFP expression, we used the pLKO.1-puro-CMV-TurboGFP_shnon-target-vector (SHC016 Sigma Aldrich), for cytosolic RFP (tdTomato) expression the LeGo-T2 vector (gift from A. Trumpp), and nuclear GFP expression (H2B–GFP) was achieved by transduction with pLKO.1-LV-GFP (Addgene 25999, Elaine Fuchs). Transduction with pLenti6.2 hygro/V5-Lifeact-YFP made it possible to image the *in vivo* dynamics of actin filaments, FUmGW (Addgene 22479, Connie Cepko) allowed *in vivo* illustration of cell membranes. Microtubuli were marked using the LentiBrite GFP-Tubulin Lentiviral Biosensor (17-10206, Merck Millipore). Lentiviral particles were produced as described before[55]. For *in vivo* tracking of Myosin II, a plasmid transfection with FuGENE HD (Promega) was performed with the Myosin-IIA-GFP vector (Addgene 38297, Matthew Krummel).

Production of lentiviral knockdowns of Cx43 (pLKO1.1-puro-CMV-tGFP-vector, Sigma Aldrich, target sequence: GCCCAAACTGATGGTGTCAAT) and GAP-43 (pLKO1.1-puro-CMV-vector, Sigma Aldrich, target sequence: TGTAGATGAAACCAAACCTAA) by shRNA technology was carried out as described before[55]. Control cells were infected with the appropriate non_target shRNA-lentiviral particles (SHC016, Sigma Aldrich). For overexpression of GAP-43, the open reading frame of GAP-43 was cloned into the pCCL.PPT.SFFV.MCS.IRES.eGFP.WPRE-vector backbone. Lentiviral particle production and transduction of target cells was done as described before[55].

Tumour cells were incubated with the harvested virus and 8 mg ml^{-1} polybrene (Merck Millipore) for 24 h. Quantification revealed a 80% protein knockdown for Cx43 and a 92.5% for GAP-43 (Western Blot analyses). If necessary, tumour cells were selected for the fluorophores by FACS sorting (BD FACSAria II Cell Sorter) or antibiotics.

For tracking of mitochondria, the BacMam 2.0 technology was used (CellLight Mitochondria-GFP, BacMam 2.0, C10600, Life Technologies).

Immunohistochemistry (IHC) and immunocytochemistry (ICC). For IHCs and ICCs, standard protocols were used. For human brain analyses, thin (3 µm) formalin-fixed paraffin-embedded human tissue sections from resected primary gliomas were obtained from the Department of Neuropathology in Heidelberg in accordance with local ethical approval. Human sections were incubated with anti-BRAF-V600E (VE1, Ventana), anti-IDH1 R132H (H09, Dianova), anti-Cx43 (C6219, Sigma), anti-GAP-43 (8945, Cell Signaling), anti-NGF (ab52918, Abcam), anti-NT4 (ab150437, Abcam), anti-TrkA (ab76291, Abcam) and anti-TrkB (ab134155, Abcam) antibodies. If not explicitly stated, all oligodendrogliomas had a 1p/19q codeletion, and all astrocytomas were non-codeleted for 1p/19q. To detect contralateral tumour cells in human brains, large sections were analysed as previously described[56].

For mouse brain analyses, animals were transcardially perfused with PBS followed by 4.5% paraformaldehyde (PFA). For ICCs, cells were grown on glass slides for 4 days and fixed with PFA. The following antibodies were used for 10 µm cryotome sections and ICCs: anti-nestin (ab6320, Abcam, specific staining of GBMSCs, no signal detectable in normal mouse brain), in combination with anti-β-catenin (ab16051, Abcam), anti-β-parvin (sc-50775, Santa Cruz), anti-beta tubulin III (ab18207, Abcam), anti-Cx26 (ab59020, Abcam), anti-Cx31 (ab156582, Abcam), anti-Cx37 (ab185820, Abcam), anti-Cx43, anti-GAP-43, anti-GFAP (Z0334, Dako), anti-Ki-67 (M7240, Dako), anti-myosin IIa (ab24762, Abcam), anti-myosin X (22430002, Novus Bioscience), anti-N-cadherin (ab18203, Abcam), and anti-PDI (ab3672, Abcam).

Photo-oxidation of GFP, and serial section scanning electron microscopy (SEM). Ten S24 GBMSC brain tumour tissue blocks were prepared for photo-oxidation as described previously[57]. Serial 70 nm thick sections of photo-oxidated epon-embedded tissue were produced using 3D SEM as described before[58]. A volume of 747 μm^3 was imaged. Specimens were imaged with a Zeiss 1530 scanning electron microscope. Images were aligned manually.

Western Blot. Western blots were performed according to standard protocols. Total protein lysates (20–50 µg) were electrophoretically separated using a 10% SDS–PAGE. After blotting and blocking, the primary antibodies (see above) were incubated over night at 4 °C. As loading control, anti-GAPDH antibody (C4780, Linaris), or anti-alpha-tubulin antibody (T9026, Sigma) was used.

Electroporation/microinjection. Horizontal acute brain slices were obtained from 2 NMRI nude mice with 131 days old S24 as described[59]. Patch electrodes with resistances of 5–10 MΩ were filled with Lucifer yellow (5 mg ml^{-1}, L0259, Sigma) and approached to identified tumour cells under visual control using a 63×, NA 1.0 dipping lens (Zeiss). The dye was transferred into tumour cells with an Axoporator 800A (Axon instruments) by 1-ms square voltage pulses at 50 Hz. Pulse amplitude was adjusted between −5 V and −20 V and train duration was adjusted up to 3 s to receive sufficient labelling of the target cell.

Image processing. MPLSM images were acquired by the ZEISS ZEN Software (Zeiss, Germany). After primary image calculation (for example, subtraction of different channels to remove unspecific background), images were transferred to Imaris (Bitplane, Switzerland) to allow 3D visualization, rendering and analysis of the data. For illustration of different aspects single planes, maximum intensity projections (MIPs) or 3D images were used. For exemplary illustration of tumour cell interconnectivity and TM branches, *z*-stacks were rendered manually (tumour cell bodies with surface function; TMs with filament tracker function). When a TM started at one cell and ended at another, these cells were defined as connected. Serial electron micrographs were reconstructed using OpenCAR software. 3D analysis of electron microscopy images was done using the Amira 5.4.6 software (Visage Imaging, Richmond, Australia). Some of the data (for example, calcium imaging) were transferred to the ImageJ software (Rasband, W.S., ImageJ, NIH). Videos were extracted from ZEN or Imaris and edited in Adobe Premiere Pro CS6.

Quantification of histology and MPLSM imaging data. In patient tumour tissue (only from primary tumour resections), maximum TM length was measured in standard 3 µm thin $IDH1^{R132H}$ IHC sections. Here, TMs were divided into 3 groups: <50 µm (not qualifying as definite TM, because other cellular structures might still be confused with filamentous structures of this length); shorter TMs of 50–100 µm, and longer TMs of >100 µm length. Quantitative analysis of human IHCs was done by a Histoscore (range 0–300) as described before[60,61].

For *in vivo* imaging data, TM numbers, branches per TM and connections per cell were counted manually, and TM lengths were measured manually in the slice mode in Imaris. Cells without a TM connection were defined as "non-connected" and cells with at least one TM-connection as "connected". TMs were also classified as connecting when the connected cell was outside the region of interest. To analyse the number of TMs before and after irradiation, the TMs of individual, identical cells were counted at both time points. The mean speed of tumour cell invasion in S24 shControl versus shGAP-43 tumours was determined by analysis of three consecutive imaging time points within a 24 h time interval *in vivo*. Distances of tumour cells to the main tumour mass (defined as a radius of 0.5 mm around the middle of the main tumour) were analysed and grouped, or displayed as individual distances to the main tumour core in tumours that were much less invasive (oligodendrogliomas). Nuclei and mitochondria (time-lapse imaging data) were marked using the spot function of Imaris. They were connected to tracks and the mean track speed was calculated. For quantification and analysis of fluorescence intensity after SR101 application, all GFP-expressing tumour cells in a volume were marked using the spot function of Imaris and then mean intensities of the SR101-channel of these spots were calculated and compared with each other. For quantification of tumour volumes two regions per animal were marked using the surface function of Imaris.

Quantification and analysis of calcium imaging data. Tumour cells and non-malignant brain astrocytes were identified by GFP/RFP expression and uptake of the chemical calcium indicator, and marked manually by the use of the region of interest manager of ImageJ. Mean grey values were measured over time. This data was processed by the program GNU Octave 3.8.1 (John W. Eaton, GPL): images were normalized to the background fluorescence using a sliding interval of ±10 images. Local maxima of calcium signals were detected by the findpeaks function (signal package, Octave-Forge). Thus the number of calcium peaks of each cell (N) could be determined and the frequency (f) was calculated. The frequency was standardized for the cell number of each region. Synchronous cells, the number of synchronous communications, and the time point of the synchronous firing were determined. Analysis was done in a window of 2 frames around each peak. This allowed to assess the synchronicity S ($S \in \mathbb{R}^+ \cup \{0\}$), which was defined by us as the fraction of the whole number of synchronous cells (N_{Syn}) divided by the number of calcium peaks for the given cell (N_{Ca}). In case the cells were not active, a synchronicity of zero was allotted.

$$\text{Synchronicity } S = \begin{cases} \frac{N_{Syn}}{N_{Ca}} & \text{for} \quad N_{Ca} > 0 \\ 0 & \text{for} \quad N_{Ca} = 0 \end{cases}$$

Hence, synchronicity states the average number of interactions at the same time point. For example, in a system with a synchronicity of 1, a firing cell interacts with a second one; for a synchronicity of 10, one cell is communicating with 10 other cells.

For the comparison between different blockers *in vivo*, the synchronicity was normalized to the baseline level. Finally, the results were summed up by a heat map. The number of calcium peaks of these cells were coded by a colour map. Synchronic cells were connected by lines, whereat the colour described the time point of the synchronic firing.

For measurement of relative changes in fluorescence intensity, tumour cells were again marked manually and relative changes were calculated ($\Delta F/F_0$). F_0 was defined as the average intensity of the 20% lowest grey values in a region of interest.

Quantification and analysis of MRI images. The slice with the largest tumour area per mouse was chosen, and both the tumour (hyperintense on T2-weighted images) and the whole brain were segmented manually. The ratio of these two areas were determined and compared between the different groups ($n = 6$ mice per group, *t*-tests).

Functional characterization of differential mRNA expression of human gliomas. RNA sequencing raw data (mapped to genes) and curated IDH-1/2 mutation data were downloaded from The Cancer Genome Atlas (TCGA) data portal on 30 January 2015, and last updated on 6 May 2015. Additionally, copy-number calls (using GISTIC 2.0) from the cBioPortal[62] and 450k- as well as CNV-NMF-clustering results from the Broad GDAC Firehose (http://gdac.broadinstitute.org/) were acquired. Only IDH mutant samples which clearly clustered to either the 1p/19q codeleted or 1p/19q non-codeleted group (and had the respective copy-number profile; 194 samples: 124 non-codeleted, 70 codeleted) were kept for further analysis. The rationale to restrict the primary analysis on *IDH* mutated gliomas was that the *IDH* mutation itself has a profound impact on epigenetic and gene expression patterns in gliomas[2,3]. First, normalization and differential gene expression analysis of RNA sequencing counts was performed using the edgeR package[63], which assumes a negative binomial distribution of count data, filtering lowly expressed transcripts. Differentially activated signalling pathways and downstream effects between codeleted and non-codeleted IDH mutated tumours were analysed with the proprietary Ingenuity Pathway Analysis (Qiagen) using a fold change filter of $|1.5|$ and FDR-q < 0.05[64] for the input list. Briefly, the software calculates both an overlap P value (based on Fisher's exact test) and an activation z score, which is based on the expression state of activating and inhibiting genes, for manually curated pathways and downstream biological functions. For this exploratory, hypothesis-generating study, results with both $P < 0.1$ and a z score $> |1.5|$ were kept.

To confirm the relevance of the results for *IDH* wild-type astrocytomas, we also analysed functional transcriptomic differences between *IDH* wild-type, non-codeleted gliomas ($n = 56$) and *IDH* mutated, 1p/19q codeleted gliomas ($n = 70$) from the TCGA RNASeq data using the analysis strategy from above. As this was a secondary, exploratory analysis, we did not perform multiple-testing adjustments for the results of our primary analysis.

Statistics. The results of image analyses were transferred to the SigmaPlot Software (Systat Software, Inc.) to test the statistical significance with the appropriate tests (data were tested for normality using the Shapiro–Wilk test and for equal variance). Statistical significance was assessed by the two-sided Student's *t*-test for normally distributed data. Otherwise a Mann–Whitney test was used for non-normal distributions. For more than two groups a one way ANOVA or an ANOVA on the ranks was performed. For contingency tables, a Fisher's exact test was used. For Kaplan–Meier survival analysis, a log rank test was performed. Results were considered statistically significant if the P value was below 0.05. Quantifications were done blinded by two independent investigators. Animal group sizes were as low as possible and empirically chosen, and longitudinal measurements allowed a reduction of animal numbers by maintaining an adequate power. No statistical methods were used to predetermine sample size. If treatments were applied, animals were randomized to these procedures. Quantitative *in vivo* data are normally depicted as mean ± standard deviation. The calculated calcium imaging frequency and synchronicity values were corrected for outliers using the Nalimov test.

49. Winkler, F. *et al.* Kinetics of vascular normalization by VEGFR2 blockade governs brain tumor response to radiation: role of oxygenation, angiopoietin-1, and matrix metalloproteinases. *Cancer Cell* **6,** 553–563 (2004).
50. Shigetomi, E., Kracun, S. & Khakh, B. S. Monitoring astrocyte calcium microdomains with improved membrane targeted GCaMP reporters. *Neuron Glia Biol.* **6,** 183–191 (2010).
51. Thestrup, T. *et al.* Optimized ratiometric calcium sensors for functional *in vivo* imaging of neurons and T lymphocytes. *Nature Methods* **11,** 175–182 (2014).
52. Lemke, D. *et al.* Primary glioblastoma cultures: can profiling of stem cell markers predict radiotherapy sensitivity? *J. Neurochem.* **131,** 251–264 (2014).
53. Kelly, J. J. *et al.* Oligodendroglioma cell lines containing t(1;19)(q10;p10). *Neuro-oncol.* **12,** 745–755 (2010).
54. Talasila, K. M. *et al.* EGFR wild-type amplification and activation promote invasion and development of glioblastoma independent of angiogenesis. *Acta Neuropathol.* **125,** 683–698 (2013).
55. Weiler, M. *et al.* mTOR target NDRG1 confers MGMT-dependent resistance to alkylating chemotherapy. *Proc. Natl Acad. Sci. USA* **111,** 409–414 (2014).
56. Sahm, F. *et al.* Addressing diffuse glioma as a systemic brain disease with single-cell analysis. *Arch. Neurol.* **69,** 523–526 (2012).
57. Horstmann, H., Vasileva, M. & Kuner, T. Photooxidation-guided ultrastructural identification and analysis of cells in neuronal tissue labeled with green fluorescent protein. *PLoS One* **8,** e64764 (2013).
58. Horstmann, H., Körber, C., Sätzler, K., Aydin, D. & Kuner, T. Serial section scanning electron microscopy (S3EM) on silicon wafers for ultra-structural volume imaging of cells and tissues. *PLoS One* **7,** e35172 (2012).
59. Geiger, J. R. *et al.* Patch-clamp recording in brain slices with improved slicer technology. *Pflugers Arch.* **443,** 491–501 (2002).
60. Bruna, A. *et al.* High TGFβ-Smad activity confers poor prognosis in glioma patients and promotes cell proliferation depending on the methylation of the PDGF-B gene. *Cancer Cell* **11,** 147–160 (2007).
61. Opitz, C. A. *et al.* An endogenous tumour-promoting ligand of the human aryl hydrocarbon receptor. *Nature* **478,** 197–203 (2011).
62. Cerami, E. *et al.* The cBio cancer genomics portal: an open platform for exploring multidimensional cancer genomics data. *Cancer Discov.* **2,** 401–404 (2012).
63. Robinson, M. D., McCarthy, D. J. & Smyth, G. K. edgeR: a Bioconductor package for differential expression analysis of digital gene expression data. *Bioinformatics* **26,** 139–140 (2010).
64. Benjamini, Y. & Hochberg, Y. Controlling the false discovery rate: a practical and powerful approach to multiple testing. *J. R. Stat. Soc. B* **57,** 289–300 (1995).

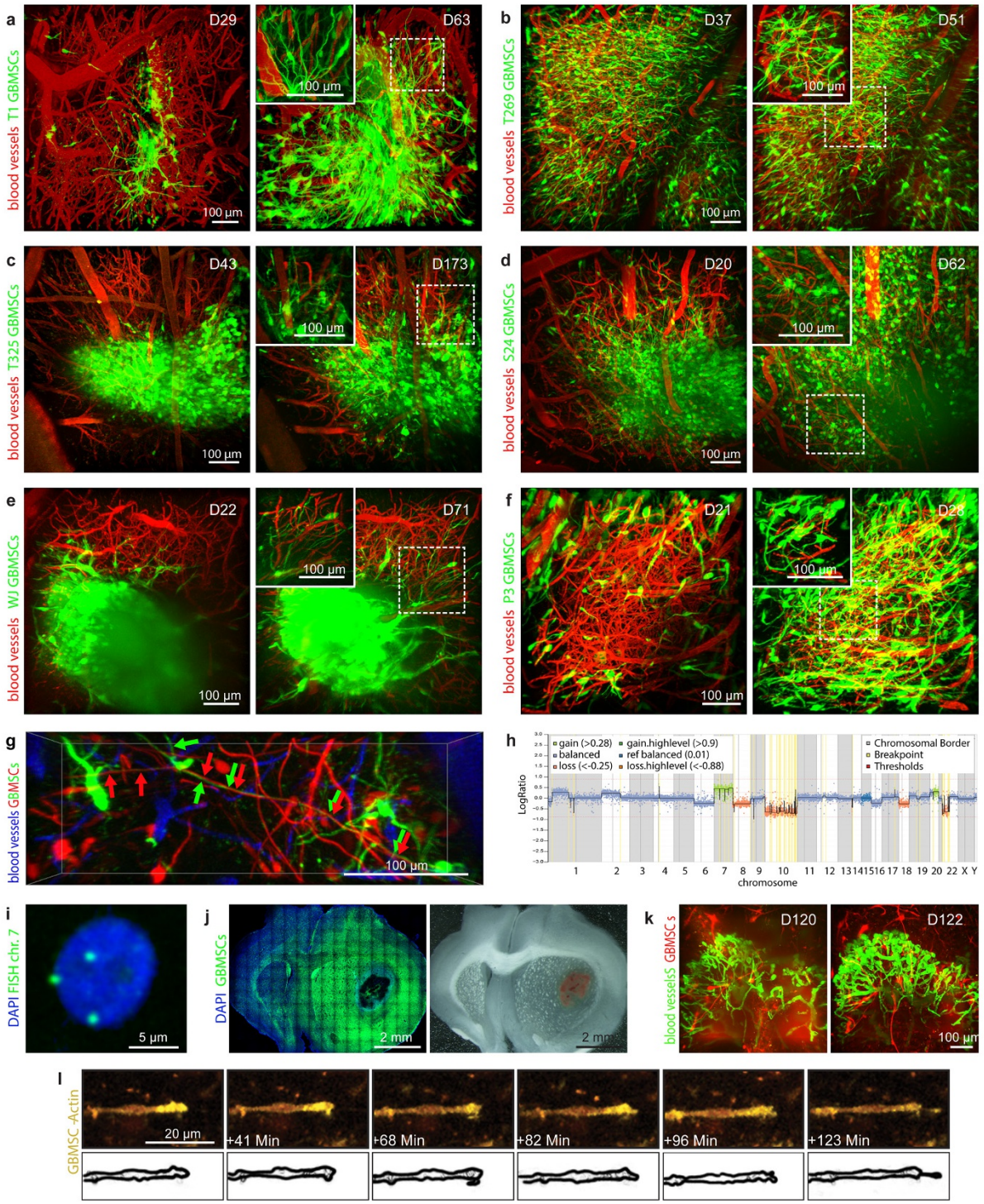

Extended Data Figure 1 | Different primary glioblastoma cell lines (GBMSCs) growing to astrocytic tumours in the mouse brain. **a**–**f**, *In vivo* microscopy (3D) of 6 different GBMSC lines (all non-codeleted for 1p/19q, and *IDH* wild-type) reveals abundant formation of ultra-long membrane protrusions in the mouse brain: T1 (**a**), T269 (**b**), T325 (**c**), S24 (**d**), WJ (**e**), and P3 (**f**) (*z*-dimensions from 200–500 µm depth). Insets show the boxed areas in the corresponding images in higher magnification, covering a proportion of the *z*-dimension. Per cell line, two time points are shown, adapted to their growth speed *in vivo* (T269, P3 fast; T1, S24 intermediate, T325 and WJ slow). **g**, 3D image of a S24 astrocytoma (injection of a 1:1 mixture of either GFP- or RFP-positive cells), revealing multiple ultra-long and very thin membrane protrusions (arrows) in the live mouse brain. Note that membrane tubes partly run in parallel. **h**, CGH-profile of the S24 GBMSC line demonstrating chromosomal alterations typical for GBM (chromosome 7 gain, 10 loss). **i**, Chromosome 7 FISH analysis of one S24 GBMSC in the main tumour area demonstrates polyploidy: 90% of $n = 100$ analysed cells in the main tumour area were clearly polyploid for chromosome 7, indicating that implanted S24 GBMSCs give rise to tumours genetically identifiable as glioblastomas. **j**, Whole mouse brain coronar sections at day 171 after S24 injection showing two main features of glioblastoma growth: diffuse brain invasion in a typical dissemination pattern (left image), and a solid, angiogenic core identified by haemorrhagic changes of the main tumour area (right bright field image). **k**, Increasing angiogenesis in this tumour is further demonstrated by dynamic *in vivo* MPLSM. **l**, Actin-rich S24 GBMSC tip, invading into the brain (single plane images; schematic drawing below). *In vivo* MPLSM: **a**–**g**, **k**, **l**.

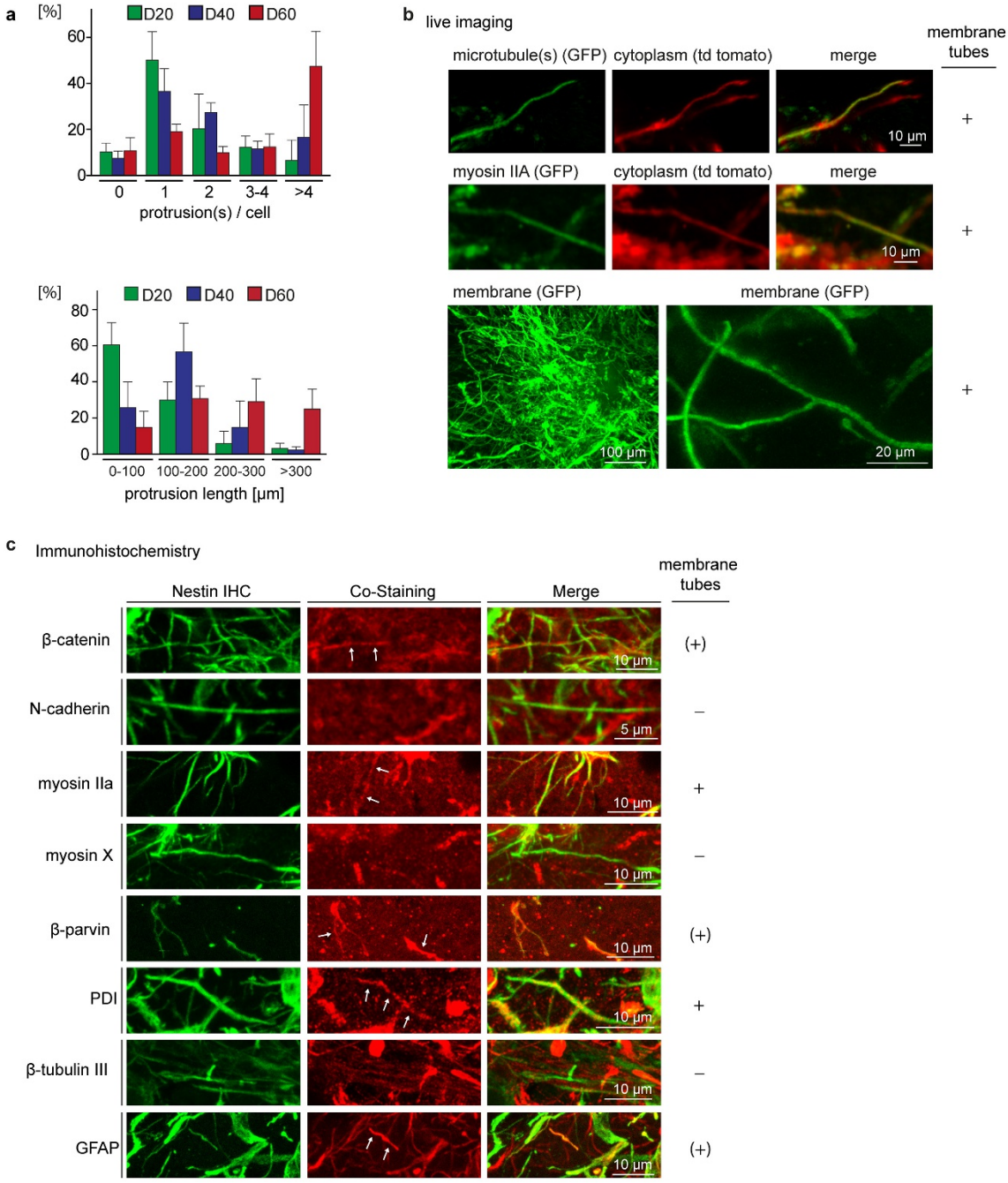

Extended Data Figure 2 | Characterization of membrane microtubes in astrocytoma mouse models. a, Number and length of protrusions during tumour progression (S24 tumours; $n = 77–120$ cells in $n = 3$ mice). **b**, MPLSM images of S24 GBMSCs genetically expressing green fluorescent protein (GFP, green) linked to different cellular/molecular components. **c**, Confocal immunohistochemistry (maximum intensity projections) of human nestin (green, allows specific detection of S24 GBMSC-related structures in the mouse brain), and different other cellular and molecular factors (red, co-stainings). The degree of expression of the factor in tumour cell-derived membrane tubes is indicated in the right lane. −, no signal in membrane tubes, (+), positive signal in some membrane tubes, +, positive signal in all membrane tubes. *In vivo* MPLSM, **a**, **b**.

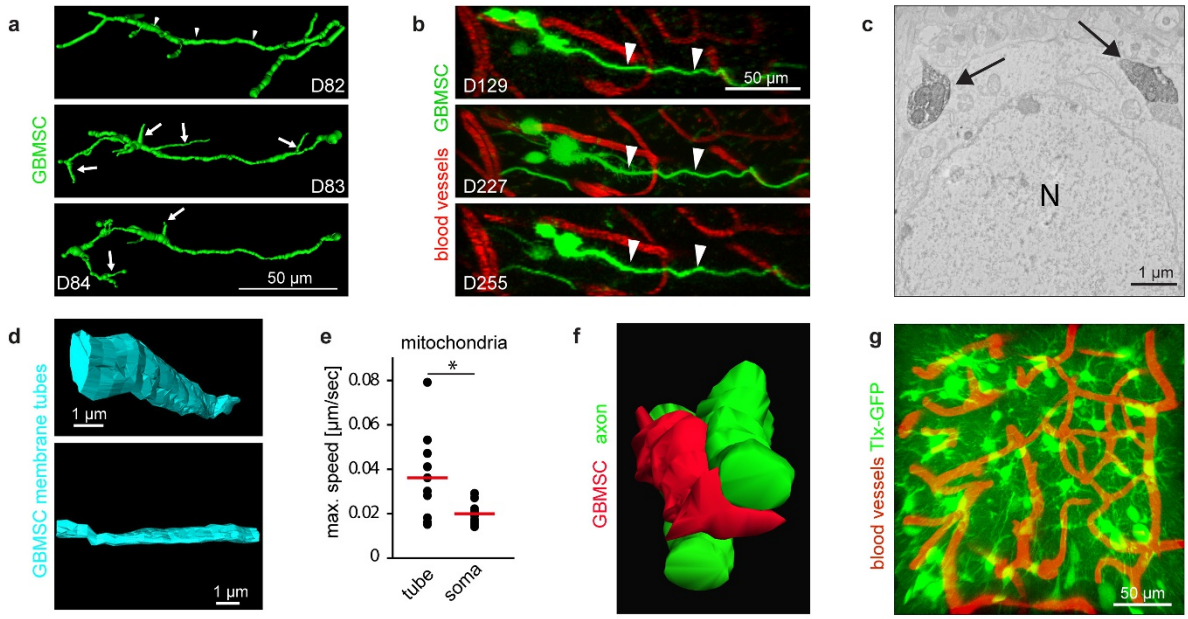

Extended Data Figure 3 | Membrane microtube dynamics and morphology. **a**, 3D reconstruction of membrane microtubes in a T325 astrocytoma over 3 days (*in vivo* MPLSM). Arrowheads, stable main tube; arrows, dynamic side tubes. **b**, Example of a very stable T325 GBMSC membrane microtube (arrowheads), followed over 126 days *in vivo*; MIP, *z*-dimension 48 µm. **c**, Scanning electron microscopy (SEM) image of two photoconverted membrane microtubes (arrows) and a nucleus of a non-photoconverted brain cell (N). **d**, 3D reconstruction of serial SEM images (22.29 µm (*xy*) × 4.62 µm (*z*) = 102.9 µm^3) illustrating the membrane contours. **e**, Maximum speed of mitochondria in S24 membrane tubes versus tumour cell soma ($n = 10$ per group, *t*-test, red lines show means). **f**, 3D reconstruction of serial SEM sections of the membrane microtube (red) and the two axons (green), which are shown in Fig. 1f. **g**, 3D image of the genetic Tlx mouse glioma model, with abundant membrane microtubes connecting single stem-like astrocytoma cells (*z*-dimension 83 µm). *In vivo* MPLSM: **a**, **b**, **e**, **g**. *$P < 0.05$.

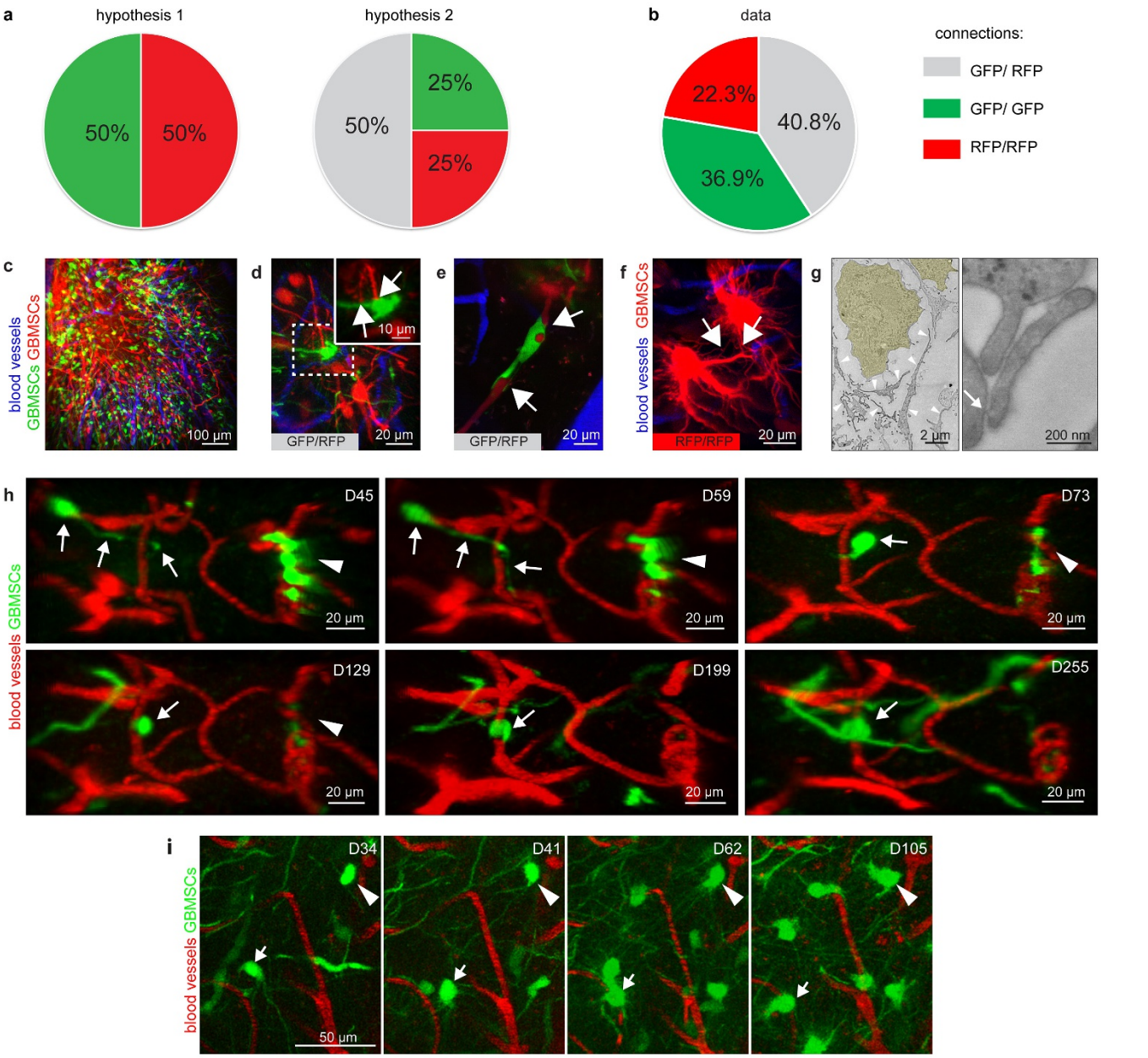

Extended Data Figure 4 | Origin of TM-connections between astrocytoma cells, and long-time tracking of TM-extending cells. **a**, Graphs illustrating two theoretically possible ways of intercellular connections by membrane tubes in a model of two tumour cell populations marked with 2 different fluorescent proteins. In hypothesis 1, tumour cells remain connected after cell division with their ancestors. In this case, only connections between cells of the same colour are expected (GFP–GFP (green) or RFP–RFP (red)). In hypothesis 2, tumour cells only connect to unrelated glioma cells. Here, 50% of connections would be between cells of different colour (GFP–RFP or RFP–GFP (grey)), and 25% of the same colour (GFP–GFP (green) and RFP–RFP (red)), respectively. **b**, Quantification of the real data set, where a 1:1 mixture of either GFP or RFP expressing S24 GBMSCs (S24GFP/S24RFP) was co-injected into the mouse brain, revealing that both potential mechanisms are in place ($n = 164$ connections in $n = 3$ mice). **c**, 3D image (70 days after injection) of a co-implantation of GFP- and RFP-expressing S24 GBMSCs. Quantification revealed that both large fluorophores (which cannot pass gap junctions) never colocalized in cell somata or in TMs ($n \geq 2{,}500$ astrocytoma cells analysed). **d**, **e**, Examples of 3D images of membrane tube connections between individual, non-related astrocytoma cells that differently express GFP or RFP (arrows in **d** and **e**). **f**, Example of a 3D image of same-colour connections between two RFP-positive cells (arrows). **g**, Scanning electron microscopy image of a S24 spheroid. Left, yellow colour marks cell bodies, arrowheads point to membrane microtubes; right, high magnification of tubes with direct membrane contact (arrow). **h**, 3D images of a perivascular T325 astrocytoma cell (arrows), which first utilizes a TM to explore the perivascular niche (D45–D73) until it moves to the explored region, and remains in a strict perivascular position until day 255. A second cell (arrowhead) is quiescent until D129 and is embedded into a vascular loop formation, which persists after disappearance of the main cell soma. **i**, MIP of a TM-containing S24 GFP astrocytoma cell which enters a perivascular position over time (arrow), and another one which remains in its non-vascular (parenchymal) position over 105 days (arrowhead). *In vivo* MPLSM, **c**–**f**, **h**, **i**; 50–650 µm deep in the brain.

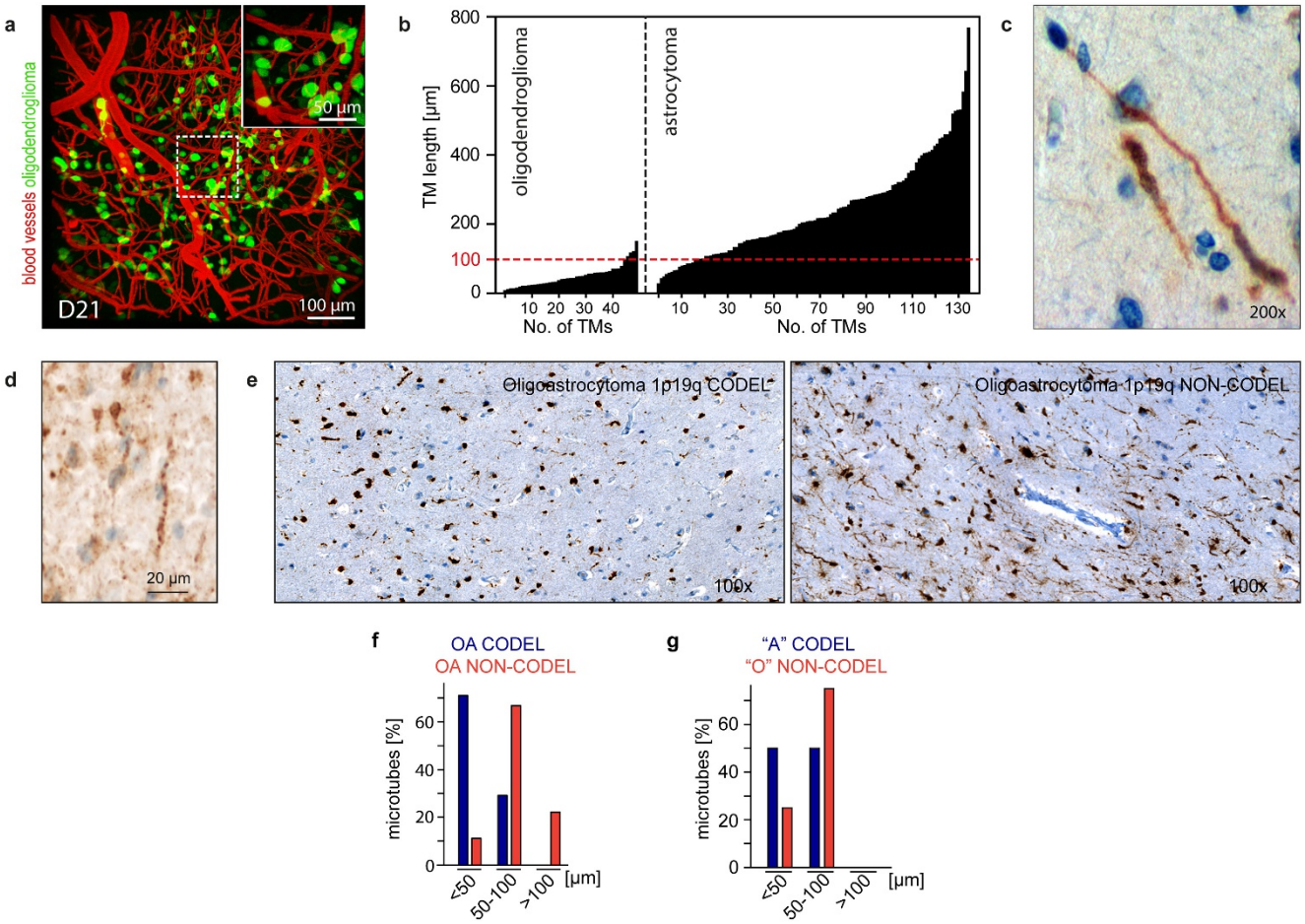

Extended Data Figure 5 | TMs in 1p/19q codeleted versus non-codeleted gliomas. a, 3D image (*in vivo* MPLSM) of a BT088 oligodendroglioma xenograft tumour growing in the mouse brain, inset shows the boxed area in a higher magnification. Cells are rounded, TMs are scarce. **b**, Quantification of TM lengths of BT088 oligodendroglioma cells (left), and S24 astrocytoma cells (right), at day 60 after tumour implantation. $n = 3$ animals per entity. **c**, $IDH1^{R132H}$ immunohistochemistry of the contralateral brain hemisphere (macroscopically tumour-free) of a patient deceased from a WHO III astrocytoma. **d**, Staining of resected primary glioblastomas ($n = 3$, non-codeleted, *IDH* wild-type) with a mutation-specific antibody against their $BRAF^{V600E}$ mutation reveals the existence of long tumour-cell-derived membrane microtubes in these tumours. Representative image. **e**, Exemplary $IDH1^{R132H}$ immunohistochemistry of gliomas morphologically classified as oligoastrocytoma, with (left) or without (right) 1p/19q codeletion. **f**, Maximum microtube length of oligoastrocytomas with 1p/19q codeletion (OA CODEL; $n = 31$ patients) and without (OA NON-CODEL; $n = 9$ patients). **g**, Maximum microtube length of tumours morphologically classified as astrocytomas but with 1p/19q codeletion ("A" CODEL; $n = 6$ patients), or classified as oligodendrogliomas but without 1p/19q codeletion ("O" NON-CODEL; $n = 9$ patients). *In vivo* MPLSM: **a**, **b**.

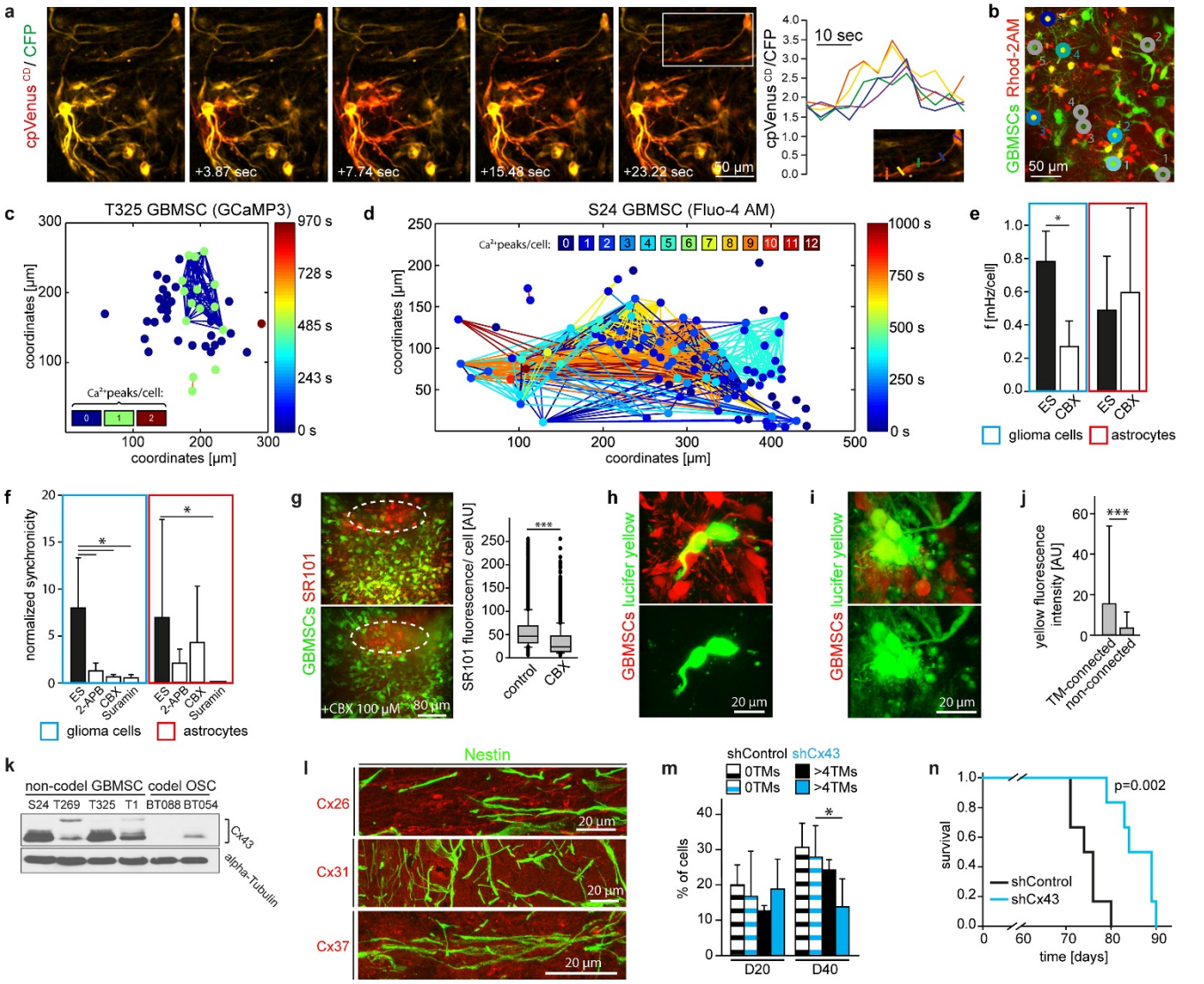

Extended Data Figure 6 | Intercellular communication via gap junctions in TM-connected astrocytoma cells, and its impact on tumour progression. a, Example of a calcium wave involving TMs of GBMSCs in a tumour region; measurement by the genetically encoded sensor Twitch-3 that allows ratiometric calcium measurements via FRET. Shown is an overlay of $cpVenus^{CD}$ and CFP channels. Yellow colour reflects low, red colour high calcium concentrations. Right: ratios of single sections of one TM illustrating the propagation of a calcium wave along the TM. **b**, MIP (10 slices) of the region shown in Fig. 2b (red cells, astrocytes; green cells, tumour cells without Rhod-2AM signal; yellow cells, tumour cells with Rhod-2AM signal). **c**, Exemplary heat map of intercellular calcium wave (ICW) communications between T325 astrocytoma cells transfected with the genetically-encoded calcium sensor GCaMP3. **d**, Heat map of the region shown in Supplementary Video 4 (small molecule calcium indicator Fluo-4AM). **e**, Frequency of calcium peaks recorded during brain superfusion with extracellular saline (ES-control) versus 100 µM carbenoxolone (CBX) in GBMSCs (blue box) and normal brain astrocytes (red box); $n = 3$ mice per group; *t*-tests. **f**, Analysis of baseline-normalized synchronicity (see Methods for details) of calcium signals between S24 GBMSC glioma cells versus those between normal brain astrocytes. Different pharmacological blockers of main propagation mechanisms of ICWs were tested: inositol triphosphate was blocked by 2-APB, cellular ATP receptors by the nonselective purinergic 2 receptor antagonist suramin, and gap junctions were blocked by CBX (glioma cells, *t*-tests; astrocytes, Mann–Whitney tests). ES, extracellular saline used as control. **g**, 3D images (*z*-dimension 180 µm) of SR101 microinjected tumours, without (control, upper image) and with co-injected CBX (lower image; area of injection: circles) 120 min. after injection. Red cells, normal brain astrocytes. Graph, corresponding quantification of SR101-fluorescence ($n = 4{,}962$–$5{,}676$ cells in $n = 3$ mice per group; Mann–Whitney test). **h**, 3D images of a non-TM-connected S24 tumour cell (S24tdTomato), loaded with the gap-junction permeable dye Lucifer yellow via electroporation. **i**, 3D images of TM-connected S24 tumour cells (S24tdTomato) after dye transfer into one of the TM-connected cells. **j**, Quantification of Lucifer yellow fluorescence intensity in the neighbouring cells next to the electroporated cell ($n = 4$ sections from $n = 2$ mice; $n = 64$ TM-connected versus $n = 42$ non-TM connected cells quantified; *t*-test). **k**, Western blot analysis of Cx43 protein expression in 4 GBMSC and 2 oligodendroglioma stem-like (OSC) cell lines. **l**, Immunohistochemistry demonstrating the localization of different connexins in S24 GBMSCs; no clear TM-related expression, and/or localization at TM crossings could be observed. **m**, Proportion of TM-devoid (0 TMs) versus TM-rich (>4 TMs) cells in shControl versus shCx43 tumours 20 and 40 days after tumour implantation ($n = 3$ mice per group, ANOVA, Tukey's post hoc test). **n**, Kaplan–Meier survival plot of animals implanted with shCx43 vs. shControl S24 GBMSCs (log rank test). **a**–**g**, **m**, Acquired by *in vivo* MPLSM. **h**, **i**, **l**, Confocal microscopy images. For gel source data, see Supplementary Fig. 1. Scale bars show s.d. $^*P < 0.05$, $^{***}P < 0.001$.

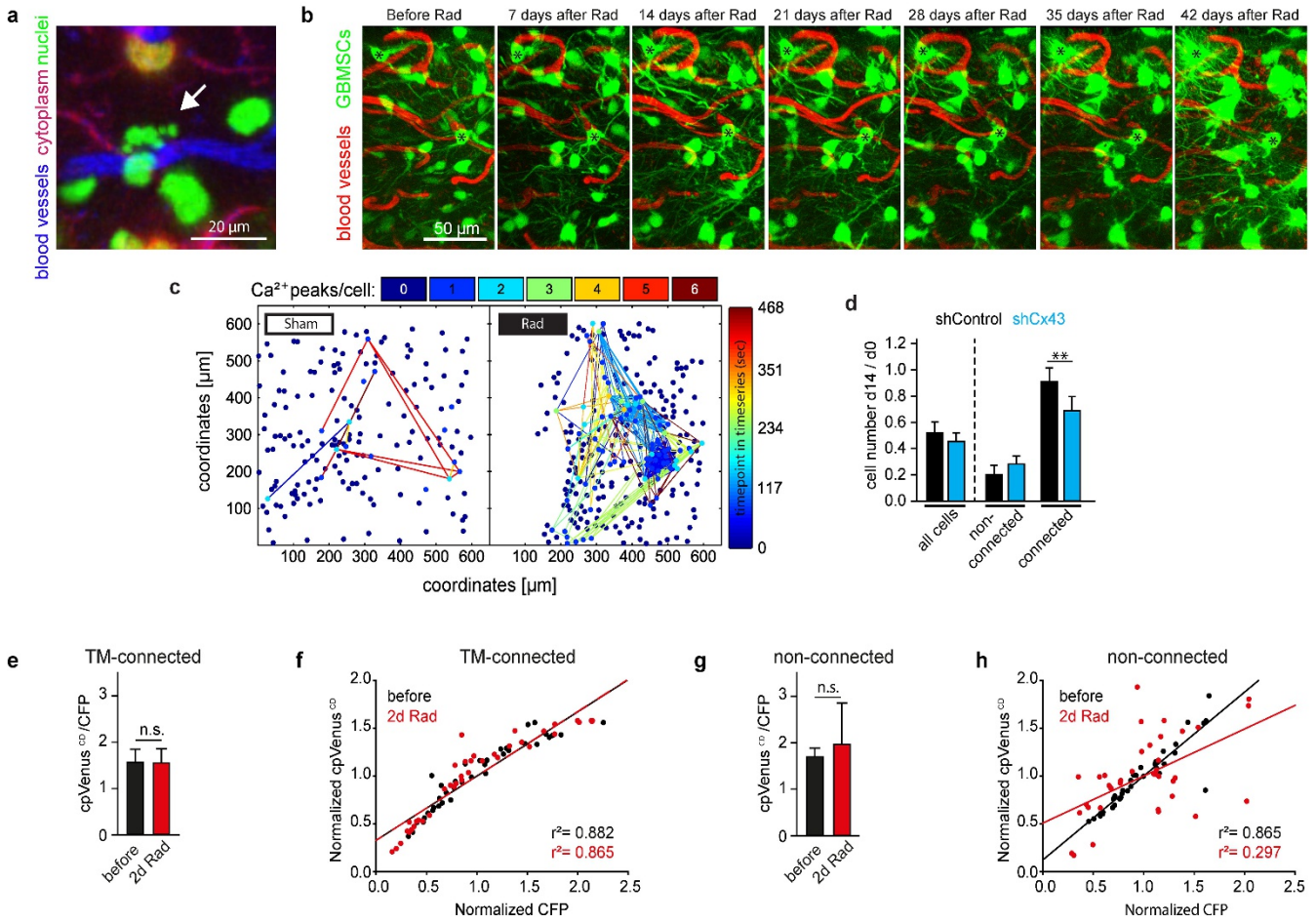

Extended Data Figure 7 | Effects of radiotherapy on cellular morphology, long-term survival, tumour cell communication, and calcium homeostasis in astrocytomas. a, 5 days after initiation of radiotherapy (3×7 Gy), nuclear fragmentation characteristic for apoptosis (arrow) can be detected in a proportion of cells. Green, nuclear staining by H2B–GFP transduction; red, S24 cell cytoplasm. **b**, Representative 42 day time course of a distinct tumour microregion, followed after start of radiotherapy (day 0). TM-connected cells (two examples are marked with black asterisks) show long-term survival; note that surviving cells show an increase in the number of their TMs. $n = 3$ mice per group. **c**, Exemplary heat maps of calcium transients (Rhod-2AM) of a sham treated (left) and radiated GBMSC tumour region (right). **d**, Relative changes of all cells (left) and subgroups of TM-connected versus non-connected GBMSCs of shControl versus shCx43 tumours after sham/radiotherapy ($n = 3$ mice per group, *t*-tests). **e**–**h**, Ratiometric measurements of basal calcium levels *in vivo*. **e**, Mean ratios of fluorescence intensities of the FRET partners cpVenus^{CD} and CFP, before, and after two days of radiation (2 × 7 Gy) in TM-connected cells ($n = 3$ mice per group; Mann–Whitney test). **f**, Fluorescence intensities (normalized by the mean intensities of the corresponding data sets) in TM-connected cells for the two FRET partners illustrated by a scatter blot (black dots represent analysed cells at the day before radiotherapy, red dots 2 days after initiation of radiotherapy); linear regression revealed similar correlation strengths at the two time points ($n = 3$ mice), reflecting very homogenous calcium levels in the astrocytoma cells before and after radiotherapy. **g**, Mean ratios of fluorescence intensities of the FRET partners before and after two days of radiation (2 × 7 Gy) in non-connected cells, $n = 3$ mice; Mann–Whitney test. **h**, Normalized fluorescence intensities in non-TM-connected cells for the two FRET partners. Here, linear regression revealed highly homogeneous basal calcium levels only before radiotherapy, while after radiotherapy the linear correlation was lost, illustrating heterogeneous calcium levels in the analysed cells. ($n = 3$ mice per group). All data acquired with *in vivo* MPLSM. GBMSCs, S24 cell line.

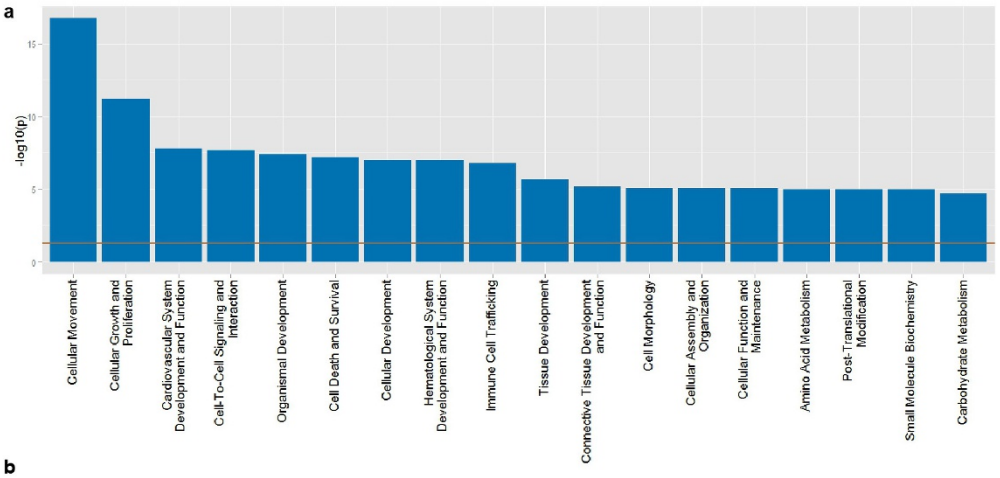

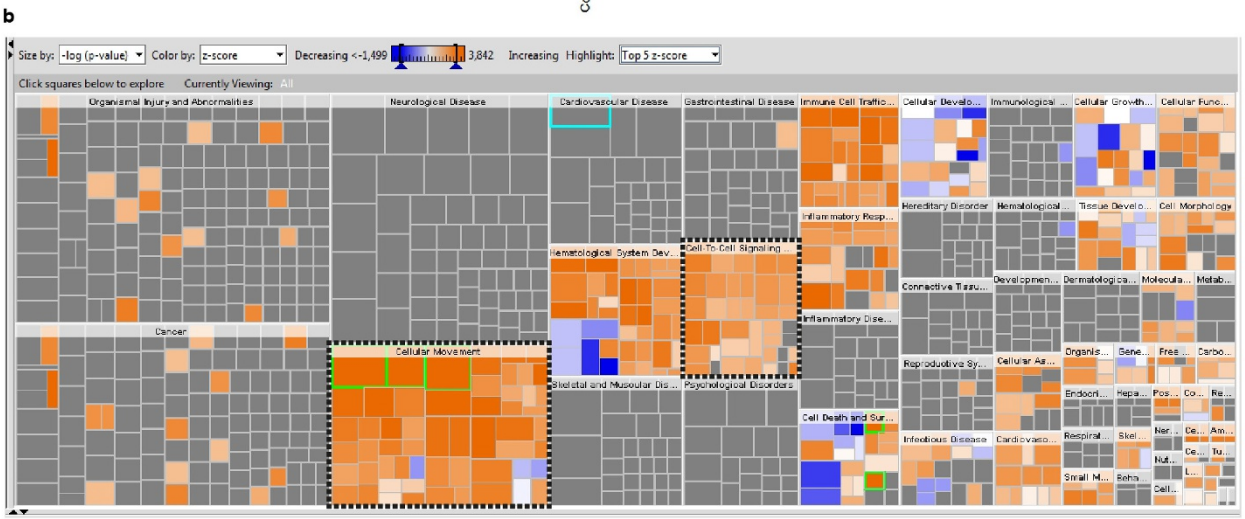

c

Ingenuity Canonical Pathways	-log(p-value)	Ratio	z-score	Molecules
Fcγ Receptor-mediated Phagocytosis in Macrophages and Monocytes	1,95E+00	1,18E-01	3,317	CDC42,SYK,INPP5D,VASP,PLD4,FYB,AKT2,ARPC1B,FCGR2A,LYN,FCGR3A/FCGR3B
IL-8 Signaling	3,88E+00	1,26E-01	3,3	JUN,IQGAP1,GNB4,MTOR,ITGB5,PLCB2,VASP,PGF,GNB1,PIK3C2B,RHOC,PLD4,ITGB2,AKT2,VCAM1,GNAI3,FOS,NRAS,GNG5,GNG4,NFKBIB,GNG12,CYBB
Acute Phase Response Signaling	2,38E+00	1,07E-01	3,207	JUN,MTOR,TF,C3,TNFRSF1A,TNFRSF1B,SERPINA3,C1R,AKT2,FOS,A2M,SOD2,NRAS,C4A/C4B,FN1,NFKBIB,FTL,C1S
Integrin Signaling	2,74E+00	1,08E-01	3,13	CDC42,ITGB5,VCL,VASP,PIK3C2B,RHOC,PARVA,PDGFB,ITGB2,ACTN1,RAP1A,AKT2,ARPC1B,NRAS,CAV1,CAPN5,ACTN2,PAK4,TNK2,ITGB4,CAPNS1
Phospholipase C Signaling	1,61E+00	8,66E-02	2,887	GNB4,PLCB2,GNB1,RHOC,PLD4,RAP1A,FCGR2A,RAPGEF3,NRAS,SYK,GNG5,GNG4,ARHGEF1,GNG12,HDAC4,HDAC9,HDAC1,ADCY8,AHNAK,LYN
Role of NFAT in Regulation of the Immune Response	4,08E+00	1,33E-01	2,887	JUN,GNB4,PLCB2,GNB1,PIK3C2B,AKT2,FCGR2A,GNAI3,HLA-DRA,FOS,NRAS,SYK,HLA-DRB1,GNG5,HLA-DMA,GNG4,HLA-DMB,NFKBIB,GNG12,CD4,LYN,FCGR3A/FCGR3B
Signaling by Rho Family GTPases	1,84E+00	9,01E-02	2,84	SEPT8,JUN,IQGAP1,CDC42,GNB4,MSN,GNB1,PIK3C2B,RHOC,ARPC1B,GNAI3,GFAP,VIM,FOS,GNG5,CYFIP1,GNG4,ARHGEF1,GNG12,PAK4,CYBB
Production of Nitric Oxide and Reactive Oxygen Species in Macrophages	2,44E+00	1,06E-01	2,828	JUN,TNFRSF1A,TNFRSF1B,APOD,PIK3C2B,JAK1,RHOC,SPI1,PPP2R2C,RAP1A,AKT2,FOS,TLR4,APOC2,PPP2R5A,NFKBIB,APOE,CYBB,CYBA
HMGB1 Signaling	1,60E+00	1,02E-01	2,714	FOS,TLR4,JUN,NRAS,CDC42,TGFB1,TNFRSF1A,TNFRSF1B,PIK3C2B,RHOC,AKT2,VCAM1
CXCR4 Signaling	2,89E+00	1,19E-01	2,673	JUN,GNB4,PLCB2,GNB1,PIK3C2B,RHOC,EGR1,AKT2,GNAI3,FOS,NRAS,GNG5,GNG4,GNG12,CD4,PAK4,ADCY8,LYN
TNFR1 Signaling	1,91E+00	1,49E-01	2,646	FOS,JUN,CDC42,TNFRSF1A,NFKBIB,CASP9,PAK4
Complement System	4,04E+00	2,50E-01	2,646	C1QC,C4A/C4B,C3,C1QB,ITGB2,C1S,C1R,C3AR1,C1QA
PKCθ Signaling in T Lymphocytes	1,08E+00	8,85E-02	2,53	FOS,JUN,NRAS,HLA-DRB1,HLA-DMA,HLA-DMB,NFKBIB,PIK3C2B,CD4,HLA-DRA
Rac Signaling	1,30E+00	9,71E-02	2,53	JUN,IQGAP1,NRAS,CDC42,CYFIP1,PIK3C2B,PAK4,CYBB,ARPC1B,CD44
MIF Regulation of Innate Immunity	1,67E+00	1,46E-01	2,449	FOS,TLR4,JUN,CD74,CD14,NFKBIB
iNOS Signaling	2,12E+00	1,63E-01	2,449	FOS,TLR4,JUN,HMGA1,CD14,NFKBIB,JAK1
IL-6 Signaling	1,02E+00	8,62E-02	2,333	FOS,JUN,A2M,NRAS,TNFRSF1A,CD14,TNFRSF1B,NFKBIB,PIK3C2B,AKT2
PI3K Signaling in B Lymphocytes	1,46E+00	9,76E-02	2,309	FOS,TLR4,JUN,NRAS,SYK,INPP5D,C3,PLCB2,NFKBIB,PLCL2,AKT2,LYN
Calcium-induced T Lymphocyte Apoptosis	1,04E+00	1,03E-01	2,236	HLA-DRB1,HLA-DMA,HLA-DMB,CD4,HDAC1,HLA-DRA
Type I Diabetes Mellitus Signaling	1,56E+00	1,04E-01	2,236	HLA-E,HLA-DRB1,HLA-DMA,TNFRSF1A,TNFRSF1B,PTPRN,HLA-DMB,NFKBIB,CASP9,JAK1,HLA-DRA
Role of Pattern Recognition Receptors in Recognition of Bacteria and Viruses	1,25E+00	9,24E-02	2,121	TLR4,C1QC,SYK,C3,TGFB1,IRF3,C1QB,PIK3C2B,RIPK2,C3AR1,C1QA
LPS-stimulated MAPK Signaling	1,38E+00	1,10E-01	2,121	FOS,TLR4,JUN,NRAS,CDC42,CD14,NFKBIB,PIK3C2B
JAK/Stat Signaling	1,41E+00	1,11E-01	2,121	FOS,JUN,NRAS,MTOR,CDKN1A,PIK3C2B,JAK1,AKT2
Paxillin Signaling	1,79E+00	1,12E-01	2,121	NRAS,CDC42,ITGB5,VCL,ACTN2,PIK3C2B,ITGB2,PARVA,ACTN1,PAK4,ITGB4
Cdc42 Signaling	2,40E+00	1,16E-01	2,121	JUN,HLA-DPB1,IQGAP1,CDC42,HLA-E,FNBP1L,ARPC1B,HLA-DRA,FOS,HLA-DRB1,HLA-DMA,HLA-DMB,HLA-DPA1,PAK4,TNK2
TNFR2 Signaling	1,21E+00	1,43E-01	2	FOS,JUN,TNFRSF1B,NFKBIB
Glioblastoma Multiforme Signaling	1,31E+00	8,97E-02	1,941	CDC42,MTOR,PLCB2,WNT5A,WNT7B,PIK3C2B,RHOC,PDGFB,FZD7,AKT2,NRAS,CDKN1A,PLCL2
PDGF Signaling	2,09E+00	1,30E-01	1,897	FOS,JUN,NRAS,CAV1,INPP5B,INPP5D,PIK3C2B,JAK1,INPPL1,PDGFB
fMLP Signaling in Neutrophils	2,31E+00	1,21E-01	1,897	CDC42,GNB4,PLCB2,GNB1,PIK3C2B,ARPC1B,GNAI3,NRAS,GNG5,GNG4,NFKBIB,GNG12,CYBB
TGF-β Signaling	1,74E+00	1,15E-01	1,89	FOS,JUN,TGFBR2,NRAS,CDC42,TGFB1,SMAD3,BMP2,HDAC1,BMP7
ILK Signaling	4,98E+00	1,38E-01	1,877	JUN,CDC42,TNFRSF1A,PGF,LIMS2,RHOC,PARVA,ITGB2,BMP2,VIM,FOS,FN1,PPP2R5A,ACTN2,FLNC,MYH7,MTOR,ITGB5,FLNA,PIK3C2B,PPP2R2C,ACTN1,AKT2,ITGB4,PPAP2B
Colorectal Cancer Metastasis Signaling	3,52E+00	1,13E-01	1,789	JUN,GNB4,TGFB1,TNFRSF1A,PRKAR2B,WNT5A,PGF,GNB1,RHOC,FZD7,TLR4,FOS,SMAD3,GNG4,ADCY8,WNT7B,CASP9,JAK1,PIK3C2B,AKT2,TGFBR2,NRAS,GNG5,GNG12,MMP24,MMP14
p70S6K Signaling	1,60E+00	1,02E-01	1,732	NRAS,SYK,MTOR,PPP2R5A,PLCB2,PIK3C2B,JAK1,PPP2R2C,PLCL2,AKT2,GNAI3,LYN
Ceramide Signaling	2,95E+00	1,50E-01	1,732	FOS,JUN,NRAS,PPP2R5A,TNFRSF1A,TNFRSF1B,SMPD3,S1PR3,PIK3C2B,PPP2R2C,AKT2,S1PR1
Renal Cell Carcinoma Signaling	2,97E+00	1,59E-01	1,667	FOS,JUN,NRAS,CDC42,TGFB1,PIK3C2B,PDGFB,ETS1,PAK4,RAP1A,AKT2
Neurotrophin/TRK Signaling	1,17E+00	1,04E-01	1,633	FOS,JUN,NRAS,CDC42,RPS6KA1,PIK3C2B,NTRK2
EGF Signaling	1,10E+00	1,07E-01	1,633	FOS,JUN,MTOR,PIK3C2B,JAK1,AKT2
IL-2 Signaling	1,64E+00	1,32E-01	1,633	FOS,JUN,NRAS,SYK,PIK3C2B,JAK1,AKT2
IL-1 Signaling	2,02E+00	1,21E-01	1,633	FOS,JUN,GNB4,GNG5,PRKAR2B,GNG4,NFKBIB,GNB1,GNG12,ADCY8,GNAI3
α-Adrenergic Signaling	2,24E+00	1,29E-01	1,633	NRAS,GNB4,SLC9A3,GNG5,PRKAR2B,GNG4,GNB1,GNG12,PIK3C1,ADCY8,GNAI3
Cardiac Hypertrophy Signaling	1,54E+00	8,64E-02	1,5	JUN,GNB4,MTOR,TGFB1,PLCB2,PRKAR2B,GNB1,PIK3C2B,RHOC,CACNA1A,GNAI3,NRAS,TGFBR2,GNG5,GNG4,RPS6KA1,GNG12,PLCL2,ADCY8
Endothelin-1 Signaling	1,72E+00	9,52E-02	1,5	JUN,EDNRA,PLCB2,EDNRB,CASP9,PIK3C2B,GUCY1A3,PLD4,GNAI3,PRDX6,FOS,NRAS,RARRES3,LCAT,PLCL2,ADCY8
Leukocyte Extravasation Signaling	3,14E+00	1,14E-01	1,5	CDC42,MLLT4,VCL,SIPA1,CD99,VASP,MSN,PIK3C2B,RAP1GAP,ITGB2,ACTN1,RAP1A,CD44,VCAM1,RAPGEF3,GNAI3,SELPLG,ACTN2,CYBB,CYBA,MMP24,MMP14
p53 Signaling	1,09E+00	9,18E-02	-1,633	JUN,CDKN1A,PIK3C2B,GADD45B,GADD45A,HDAC9,AKT2,HDAC1,TNFRSF10B
RhoGDI Signaling	1,35E+00	8,72E-02	-2,333	CDC42,GNB4,MSN,GNB1,RHOC,ARPC1B,CD44,GNAI3,ARHGDIB,GNG5,GNG4,ARHGEF1,GNG12,PAK4,WASF2
PPAR Signaling	1,28E+00	1,00E-01	-2,828	FOS,JUN,NRAS,PPARGC1A,TNFRSF1A,TNFRSF1B,NFKBIB,NR2F1,PDGFB
PPARα/RXRα Activation	1,21E+00	8,48E-02	3	JUN,ITGB5,TGFB1,PLCB2,PRKAR2B,FASN,NRAS,TGFBR2,PPARGC1A,SMAD3,NFKBIB,NR2F1,PLCL2,ADCY8

Extended Data Figure 8 | *In silico* analysis of 1p/19q codeleted versus non-codeleted *IDH* mutated human gliomas. Biological function analysis of 1p/19q non-codeleted ($n = 124$) versus 1p/19q codeleted ($n = 70$) human gliomas of the TCGA database was performed using Ingenuity Pathway Analysis. All tumours analysed were *IDH* mutated (GCIMP+). **a**, Bar plot of the top differentially regulated downstream biological functions. **b**, Heat map of downstream biological functions. The map is colour coded: more intense orange means more activation in 1p/19q non-codeleted tumours (compared to codeleted tumours), blue the other way round. Note the activation of "cellular movement" and "cell-to-cell signaling" in non-codeleted tumours. **c**, Results of the analysis of canonical pathways in 1p/19q non-codeleted versus codeleted gliomas. Higher positive z-score: upregulated in 1p/19q non-codeleted versus codeleted gliomas; higher negative z-score: upregulated in 1p/19q codeleted gliomas versus non-codeleted gliomas.

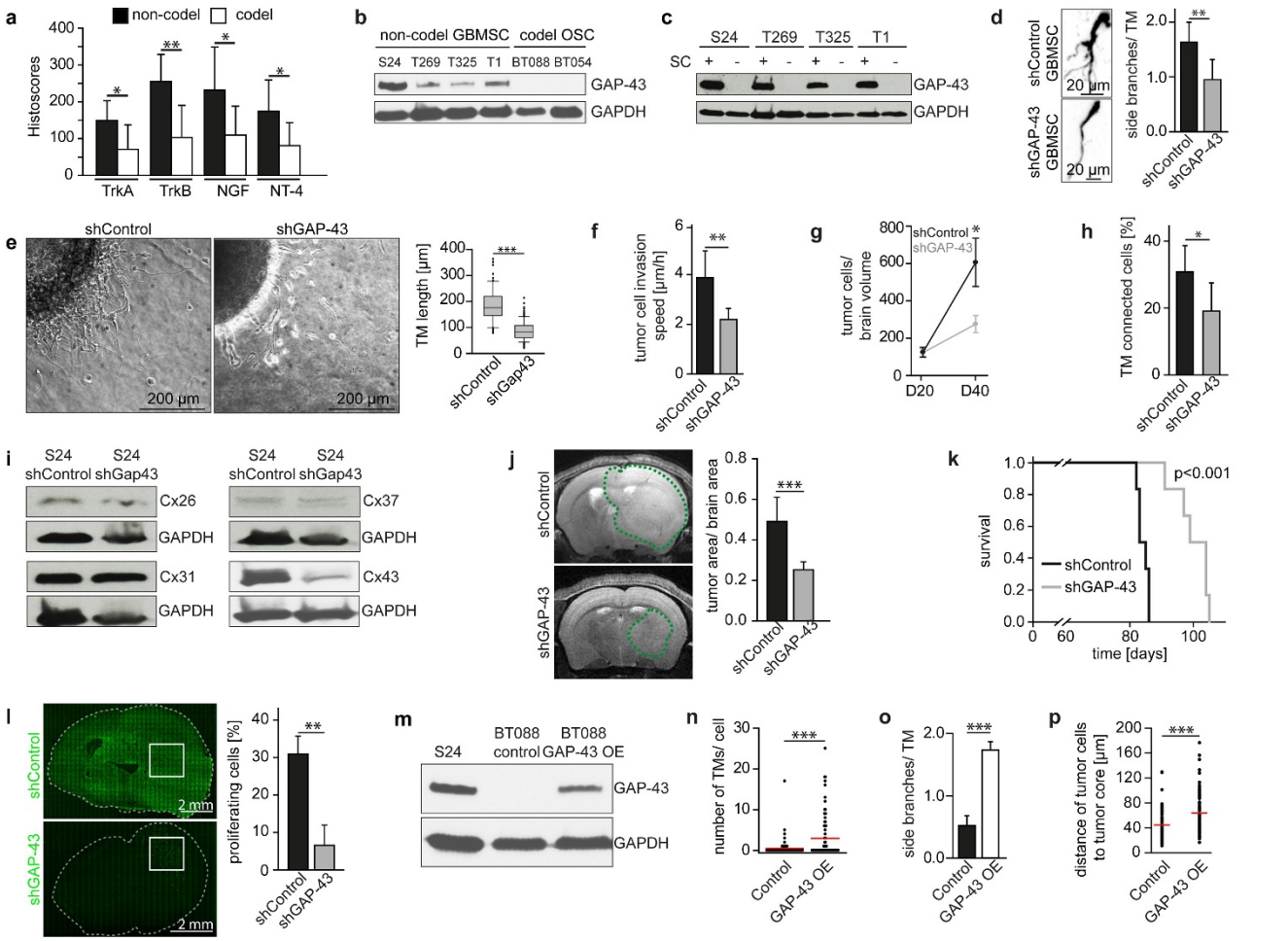

Extended Data Figure 9 | Proficiency for GAP-43 expression drives malignant features associated with TMs. a, TrkA, TrkB, NGF and NT-4 protein expression detected by immunohistochemistry in 1p/19 codeleted versus non-codeleted human gliomas ($n = 8$ each, *t*-tests, all *IDH* mutated). **b**, Western blot analysis of GAP-43 protein expression of different glioma cell lines. OSC, oligodendroglioma stem-like cell lines. **c**, GAP-43 western blot of 4 GBMSC lines cultured under non-adherent, stemlike (SC +) versus differentiating, serum-containing, adherent (SC −) conditions. **d**, *In vivo* 3D images of S24 shControl versus shGAP-43 GBMSCs (left) and quantification of TM side branches 20 days after implantation ($n = 60$ cells in $n = 5/6$ mice, *t*-test). **e**, Spheroid invasion assay from S24 shControl versus shGAP-43 cells in a gel matrix, and the corresponding quantification (*t*-test). **f**, *In vivo* tumour cell invasion distance within 24 h of S24 shControl versus shGAP-43 GBMSC tumours ($n = 3$ mice, Mann–Whitney test). **g**, *In vivo* proliferation dynamics in the main tumour area (volume of 0.037 mm^3; $n = 4$ mice, Mann–Whitney tests). **h**, Fraction of TM-connected cells at day 20 in these tumours ($n = 164$ cells in $n = 6$ mice, *t*-test). **i**, Western blot analysis of Cx26 (expressed in normal astrocytes), Cx31 and Cx37 (both located on chromosome 1p), and Cx43 protein expression in shGAP-43 GBMSCs versus shControls. Of note, the GAP-43 knockdown leads to a Cx43 protein reduction of 89%, while expression of the other connexins was not reduced. **j**, T2 MRI images of S24 shControl versus shGAP-43 tumours, 72 days after tumour implantation. Quantifications of $n = 6$ animals per group (*t*-test). **k**, Kaplan–Meier survival plot of S24 shControl versus shGAP-43 tumour-bearing mice (log rank test). **l**, Exemplary brain sections with nestin immunohistochemistry of S24 shControl versus shGAP-43 tumours 60 days after radiotherapy. Note that in shGAP-43 tumours, only small remnants of tumour cells can be detected by the tumour cell-specific staining. Regions with highest tumour cell densities (boxes) were quantified for proliferation index (Ki-67-positive cells/all cells; $n = 3$ animals; *t*-test). **m**, Overexpression of GAP-43 in BT088 oligodendroglioma cells results in protein levels similar to that in GBMSCs. **n**–**p**, GAP-43 overexpression in BT088 oligodendroglioma cells leads to an increase in TM numbers (**n**, $n = 80$ cells in $n = 3$ mice per group), more TM branches (**o**, $n = 40$ cells in $n = 3$ mice per group), and a higher invasion capacity (**p**, $n = 75$ cells in $n = 3$ mice per group; *t*-tests) 14 days after tumour injection. Scale bars show s.d. Red lines show means. *In vivo* MPLSM, **d**, **f**–**h**, **n**–**p**. For gel source data, see Supplementary Fig. 1. $^*P < 0.05$, $^{**}P < 0.01$, $^{***}P < 0.001$.

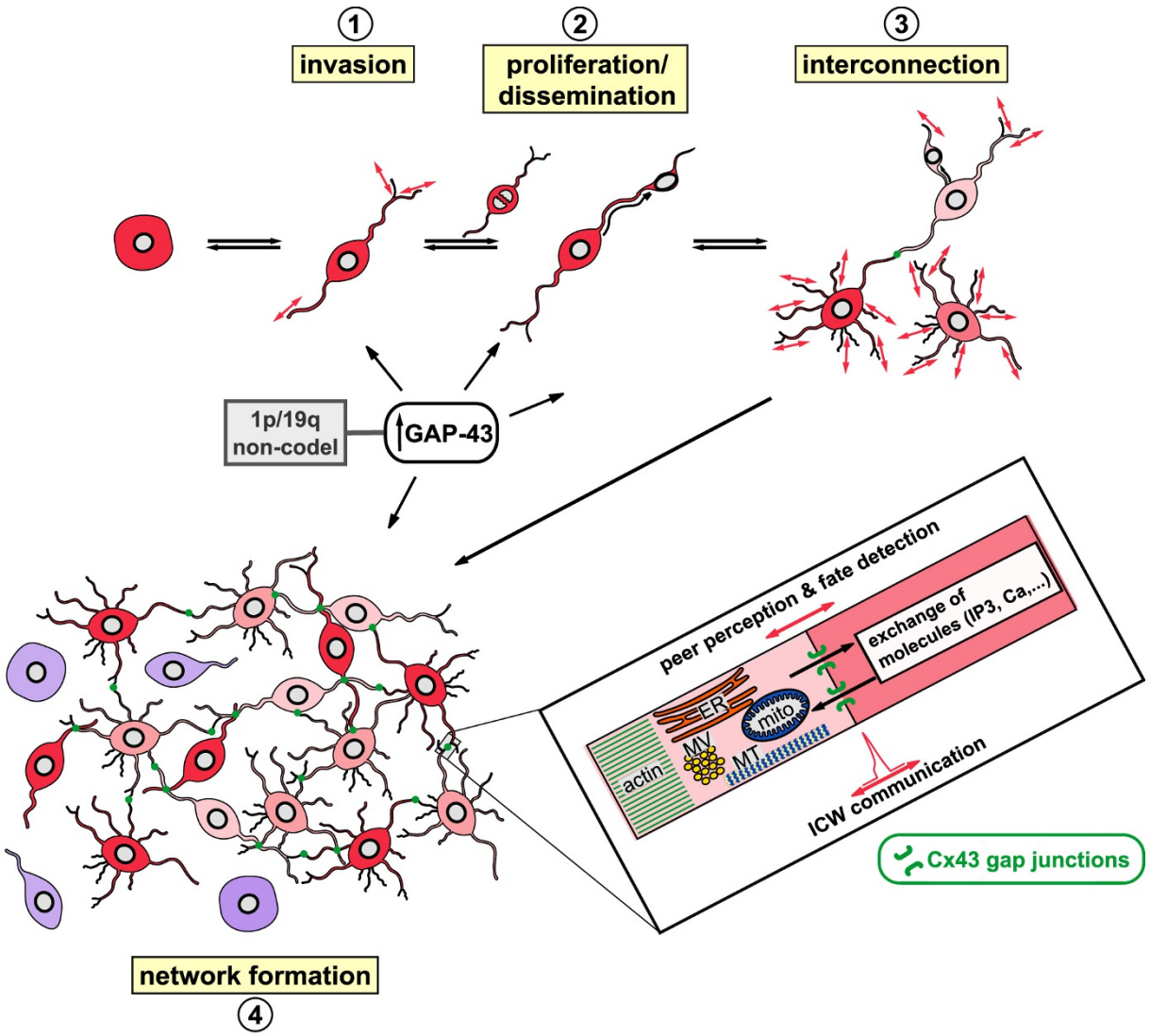

Extended Data Figure 10 | Schematic illustration of the role of TMs in brain tumour progression. Anatomical and molecular mechanisms of TM-driven tumour dissemination and network function in astrocytomas. MV, microvesicles; mito, mitochondrion; ER, endoplasmic reticulum; MT, microtubules.